Application of fluorescent-tagged antiscalants for mitigation of membrane scaling by calcium carbonate and calcium phosphate in electrodialysis stack

V. Gil,[1]* M. Porozhnyy,[1] M. Oshchepkov,[2] V. Ruleva,[1] A. Ryabova,[3] M. Trukhina,[4] S. Tkachenko,[2] N. Pismenskaya[1] and K. Popov[4]**

[1]Kuban State University, 149 Stavropolskaya Str., 350040 Krasnodar, Russian Federation
[2]Mendeleev University of Chemical Technology of Russia, Miusskaya Sq. 9, 125047 Moscow, Russian Federation
[3]Prokhorov General Physics Institute of the Russian Academy of Sciences, Vavilov Str., 38, 119991 Moscow, Russian Federation
[4]JSC "Fine Chemicals R&D Centre", Krasnobogatyrskaya, Str. 42, b1, 107258 Moscow, Russian Federation
*E-mail: *violetta_gil@mail.ru; **ki-popov49@yandex.ru*

Abstract

Wide application of electrodialysis, which is proven to be highly effective in waste waters treatment and in a broad spectrum of other technologies, is restrained by membrane fouling. The present study is dedicated to the application of fluorescent-tagged antiscalants (ASs) for mitigation of membrane scaling by calcium carbonate and calcium phosphate in the electrodialysis stack within a set of model experiments. Hydroxyethylidenebis(phosphonic acid), conjugated with naphthalimide (HEDP-F), and two fluoresceine-tagged polyacrylates (PAA-F2 and PAA-F2S) are tested. It is demonstrated that all three ASs are highly efficient in $CaCO_3$ scaling retardation: PAA-F2S > PAA-F2 > HEDP-F. The similar efficiency is found for the case of $CaHPO_4 \cdot 2H_2O$: PAA-F2S > PAA-F2 >> HEDP-F. At the same time, PAA-F2S and PAA-F2 affect the crystal habit of both $CaCO_3$ and $CaHPO_4 \cdot 2H_2O$, while HEDP-F does not. However, due to the visualization of antiscalants it is found that there is no direct relevance between scale inhibition efficacy and an ability of ASs to affect the $CaCO_3$ crystal growth kinetics and the crystal form of a deposit. The major scaling inhibition effect is detected at the nucleation step: an increase of induction time. However, no definite decrease of the crystal growth rate at the stages following nucleation is registered relative to the blank run. Meanwhile, most of AS molecules are found to stay in aqueous phase till the end of scale formation and only then do they begin to get adsorbed by the deposit. Notably, in the case of $CaCO_3$, PAA-F2S and PAA-F2 reveal selective sorption on vaterite, a bit less intensive sorption on flake-like modification of calcite and the least sorption on rhomboherdal modification of calcite surfaces. In the same way, PAA-F2S and PAA-F2 demonstrate location on plate-like modifications of $CaHPO_4 \cdot 2H_2O$, but reveal no presence on the pellet-like modifications of this mineral. It is shown that there is no direct correlation between location of ASs and crystal growth rate. The observed effects are interpreted in terms of AS interactions with natural nanoimpurities acting as crystallization centers at the nucleation step.

Received: December 1, 2023. Published: March 2, 2024 doi: 10.17675/2305-6894-2024-13-1-24

Keywords: *electrodialysis, scaling, scale inhibition, fluorescent-tagged antiscalants, antiscalant visualization, chronopotentiometry, fluorescence microscopy, calcium carbonate, calcium phosphate, polyacrylate, bisphosphonate.*

1. Introduction

Membrane technologies have been utilized for the treatment of natural and wastewaters since 1960 [1]. Presently, membrane desalination accounts for up to 3/4 of global desalination capacity with reverse osmosis (RO) being the most popular method [2]. However, using RO is economically justified only to obtain weakly concentrated retentates, whose discharge causes irreparable damage to the environment [3]. To demineralize solutions containing less than 7–10 g/dm^3 of salts, the method of electrodialysis (ED) is preferable to RO from the economic point of view [4]. At the same time, ED allows to concentrate solutions of mineral salts up to values of 150–250 g/dm^3. This provides great opportunities for the processing of RO retentates [5–7], contributing to the cost reduction and environmental feasibility of hybrid technologies as well as the development of zero liquid discharge (ZLD) technology processes [8, 9].

Currently, electrodialysis has proven to be highly effective in concentrating, separating and selectively extracting valuable components from mine waters, natural brines [10, 11] and liquid media of the dairy industry (whey, *etc*.) [12, 13], in adjusting quality of juice and wine [14, 15]. These liquid media typically contain hardness cations (calcium, magnesium) and anions of sulfuric, carbonic, phosphoric acids, which tend to precipitate as a result of exceeding the solubility product due to the ion transfer through membranes [16]. Furthermore, in the case of ED, a local pH shift at the surfaces of ion-exchange membranes (IEMs) can be caused by water splitting induced by the electric current flow. Precipitation/sedimentation results in scaling (mineral fouling), which blocks part of the surface and clogs the pores of IEMs. This in turn leads to an increase in resistance, a decrease in permselectivity, and to a change in a number of other membrane properties [16, 17]. These phenomena are causing a decrease in current efficiency and an increase in energy consumption. The expenses for membrane regeneration and replacement may reach up to almost 50% of the total cost [18]. As a result, IEM fouling impedes the expansion of eco-friendly, resource-conserving ED technologies. Thus, for example, ED desalination constitutes merely 4% of the worldwide desalination capacity [19].

Several reviews [17, 20–24] focus on the problem of fouling in electrodialysis processes and the existing approaches to deal with it. The conventional method to mitigate fouling is electrodialysis reversal (EDR), which by the 1970s was extensively tested and successfully deployed at an industrial scale [25]. Despite numerous studies and a certain success in determining the optimal EDR process parameters for reducing fouling potential (current density and polarity change frequency, hydrodynamic parameters, *etc*.) [26], this method has a major drawback: it leads to significant losses of the final product.

Among other methods for controlling fouling in ED, the relatively recent technologies of metathesis ED and selectrodialysis are of particular interest. Metathesis ED involves a specific configuration of the membrane stack and addition of a substitution solution to provide the exchangeable ions for the metathesis reaction. This ensures an organization of ion fluxes in which each concentration compartment tract contains only components that are not prone to precipitate formation [27]. In selectrodialysis, the separation of ions capable of forming sparingly soluble compounds is carried out using a specially designed electrodialysis unit with membranes that are selective for singly-charged ions [28]. Thus, these recent technologies require a considerable complication in the design of electrodialyzers and hydraulic circuits, as well as the use of special ion-exchange membranes.

A commonly employed method to tackle fouling is the application of non-stationary electric current regimes such as pulsed electric field (PEF) [12, 29, 30]. The PEF method consists in alternating pulse and pause lapses of electric current and is used in standard ED cells without requiring additional transformation [31]. The method allows suppressing membrane fouling (both mineral [12, 29, 31] and organic [29, 30, 32, 33]) while also delivering high final product yields with relatively low energy consumption. However, this method is not universal and, in each specific case, its parameters must be thoroughly adjusted for successful implementation.

The method of adding scale inhibitors (antiscalants) to solutions being processed is very simple in terms of technical design and is actively used in baromembrane processes [34, 35], but has not been widely implemented in electrodialysis. In scientific literature, there are only few reports on successful application of antiscalants in ED [36–40]. At the same time, these studies simply represent the demo-case of antiscalant's positive effect without considering inhibition mechanisms whatsoever. Therefore, the behavior of antiscalants in ED processes have not been systematically studied, despite the substantial potential for using these substances to combat scaling.

Commercially available antiscalants (ASs) are represented by three groups of substances [35]: phosphates (polyphosphates), phosphonates and polycarboxylates. Phosphates were the first antiscalants to be introduced to the membrane industry [41]. Later, phosphate ASs were replaced by phosphonates and polycarboxylates (such as polyacrylate, polymaleate, *etc*.), which are widely used in water treatment technologies due to their superior scale inhibition efficiency [42, 43]. One of the key advantages of antiscalants is the low concentrations required (*i.e*., sub-stoichiometric amounts), which reduces the effect of the antiscalant presence on the quality of the treated liquid media [35, 44]. Additionally, if needed, these substances can be removed from the final product [45].

In general, the following inhibition mechanisms of antiscalants are recognized [16, 35]:

1. threshold homogeneous inhibition: a sub-stoichiometric amount of ASs retards crystal growth or precipitation due to hindering of the homogeneous nucleation step;

2. crystal structure modification: change in the orderly growth of a scale crystal makes it deformed and leads to slower growing due to irreversible adsorption of ASs by the most active crystal growth centers (kinks, steps, or selected edges);
3. dispersion: the retardation of crystal aggregation caused by the adsorption of ASs on crystals imparts their surface charge and provides electrostatic repulsion;
4. chelation: making cations of sparingly soluble salts unavailable for scaling by forming their soluble complexes with ASs (this mechanism is meaningful either at low supersaturation, or at high (non sub-stoichiometric) ASs concentrations).

Differentiating and assessing the contribution of each mechanism in the total inhibition effect is a highly challenging task. At the same time, this classification of ASs inhibition mechanisms cannot be considered as comprehensive, since it does not provide a satisfactory explanation to a sufficient amount of contradictions currently existing in literature [46]. In this regard, any information that provides analysis of the effect of antiscalants in a specific situation is highly valuable. The development of new scale inhibitors with fluorescent properties opens up new prospects for addressing this issue [47–49]. The addition of fluorescent fragments to antiscalant structure presents a novel means of monitoring their impact on scale formation processes. The results obtained from static (beaker tests) and dynamic (reverse osmosis) experiments with such ASs lead to a hypothesis attributing the decisive role in scale crystals formation to solid impurities (with particle size <200 nm) acting as crystallization centers [46, 48]. According to this hypothesis, the main mechanism of antiscalant action consists in blocking the surfaces of these impurities.

Our recent studies [50, 51] present the first instance of the examination of new antiscalants HEDP-F (fluorescent-tagged bisphosphonate) and PAA-F2 (fluorescent-tagged polyacrylate) in the ED processing of the solutions prone to calcium sulfate scale formation. It was found, that both ASs are capable of scaling mitigation on the surface of cation-exchange membranes facing the concentration compartment. Polymeric AS PAA-F2 proved to be more efficient than HEDP-F, significantly preventing scale deposition on the membrane surface during the three-hour electrodialysis experiment. The complex of the results obtained, including fluorescence and scanning electron microscopy data, allowed us to conclude, that the main mechanism of ASs action in the studied ED system is the same as suggested by the above-mentioned hypothesis [46, 48].

In addition to calcium sulfates, calcium carbonates and calcium phosphates must be considered among the most common scale-forming components in water treatment membrane processes [52], since this compounds are abundant in municipal and industrial wastewater, as well as in natural waters being processed. Thus, it is of great interest to examine the prospects of various antiscalants application, and to study the peculiarities of their action in electrodialysis processing of liquid media prone to the formation of calcium carbonates and calcium phosphates deposits. In this research, such investigation will be conducted for the first time. The behavior of three fluorescent-tagged antiscalants will be studied: naphthalimide-tagged bisphosphonate HEDP-F, fluorescein-tagged polyacrylate

PAA-F2, and a newly developed fluorescein-tagged polyacrylate PAA-F2S with specially grafted sulfo groups for better dispersion of AS in the solution (Figure 1).

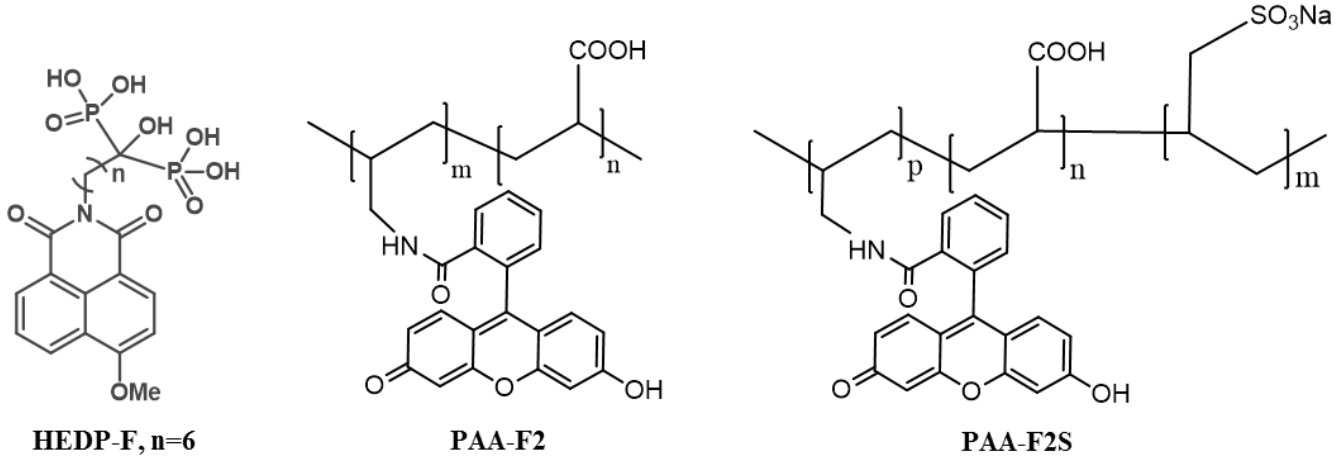

Figure 1. HEDP-F, PAA-F2, and PAA-F2S molecular structures.

The key objectives of the present study are: (*i*) to estimate the effectiveness of the studied antiscalants against calcium carbonate and calcium phosphate scaling in concentration compartments of electrodialysis systems; (*ii*) to test a new fluorescent antiscalant containing sulfo groups and asses its effects in comparison with two other fluorescent scale inhibitors; (*iii*) to gain insight into the inhibition mechanisms in the studied electrodialysis systems *via* visualization of fluorescent-tagged antiscalants.

2. Experimental

2.1. Reagents

The synthesis of fluorescent-tagged antiscalants HEDP-F (molecular mass 559 Da) and PAA-F2 (molecular mass 4000 Da) is described in [47] and [53], respectively, while PAA-F2S (molecular mass 4000 Da) was synthesized by microfluidic method according to [54]. HEDP-F exhibits the blue light emission (fluorescence band at 460 nm), while PAA-F2 and PAA-F2S provide green fluorescence (fluorescence band at 505 nm).

It is important to mention that although antiscalants, based on naphthalimide, display fluorescence in the blue spectral range, the green pseudo-color is used to represent the fluorescent channel for HEDP-F in this paper for readers' convenience, since humans perceive green color in the wider dynamic range compared with blue.

For the preparation of stock solutions, deionized water (electrical conductivity was 2.3 ± 0.1 $\mu S \cdot cm^{-1}$) and commercial solid NaCl, $CaCl_2$, $NaHCO_3$, NaH_2PO_4 (reagent grade; manufacturer: Vecton JSC) are used.

2.2. Membranes

In this research, two commercial heterogeneous membranes manufactured by Shchekinoazot Ltd., Russia, are used: a cation-exchange membrane (CEM) MK-40 as the studied membrane and an anion-exchange membrane (AEM) MA-41 as the auxiliary membrane. The membranes are produced by hot rolling of a mixture of polyethylene (inert binder) and powdered KU-2 (MK-40) or AV-17 (MA-41) ion-exchange resin (styrene-divinylbenzene copolymer) containing fixed functional sulfo or amino groups, respectively. Particles of the ion-exchange resins, protruding from the polyethylene surface, provided selective conductivity of the membranes. The membranes contain the reinforcing cloth of polyamide filaments [55].

Our previous study [50] has revealed that the MK-40 membrane exhibits auto-luminescence in the broad spectrum, ranging from 460 to 650 nm. Fluorescent microscopy images of this membrane showed that the fluorescence is attributed to the grains of the ion-exchange resin and is tentatively conditioned by the presence of the styrene-divinylbenzene copolymer in its structure.

Luminescence spectrum of the studied membrane overlaps with fluorescence bands of the ASs used it this research, which hinders ASs tracing on the MK-40 surface. On the other hand, it is possible to detect the ASs under study against the dark deposit layer, which screens the membrane luminescence. Thus, the location of antiscalant on the surface of scale layer becomes feasible.

2.3. Electrodialysis experiments

Two series of three-hour long experiments on the electrodialysis processing of solutions prone to forming scales of calcium carbonate or calcium hydrogen phosphate are conducted. The four-compartment flow electrodialysis cell, used in the present study, is schematically shown in Figure 2. The ED cell consists of desalination compartment (DC), concentration compartment (CC) and two electrode compartments (EC). The studied CEM MK-40 and two auxiliary AEMs MA-41 form the DC and CC of the cell with the 6.6 mm intermembrane distance, and 4.3 cm^2 active membrane area. Luggin's capillaries, that are brought to the geometric center of the studied membrane on its both sides, are connected with Ag/AgCl electrodes and used to measure the potential drop (PD) across the membrane by the multimeter Keithley 2010 (Keithley Instruments, Inc., USA). The constant current of the twofold limiting current value is supplied to the cell using the programmable power supply Keithley 2200-60-2 (Keithley Instruments, Inc., USA). Such overlimiting current mode is applied in order to intensify the process of scale formation in the systems under study. The limiting current values for each of two studied systems are determined experimentally *via* acquiring voltamperograms.

In the first series of the ED experiments, the 0.04 mol/dm^3 $CaCl_2$ solution (volume 4 L) circulates through the DC, the 0.04 mol/dm^3 $NaHCO_3$ solution (volume 4 L) is pumped through the CC. At the same time, the 0.04 mol/dm^3 NaCl solution (volume 4 L) circulates

through the electrode compartments. The constant linear flow rate of the solutions in each compartment is set equal to 0.4 cm/s.

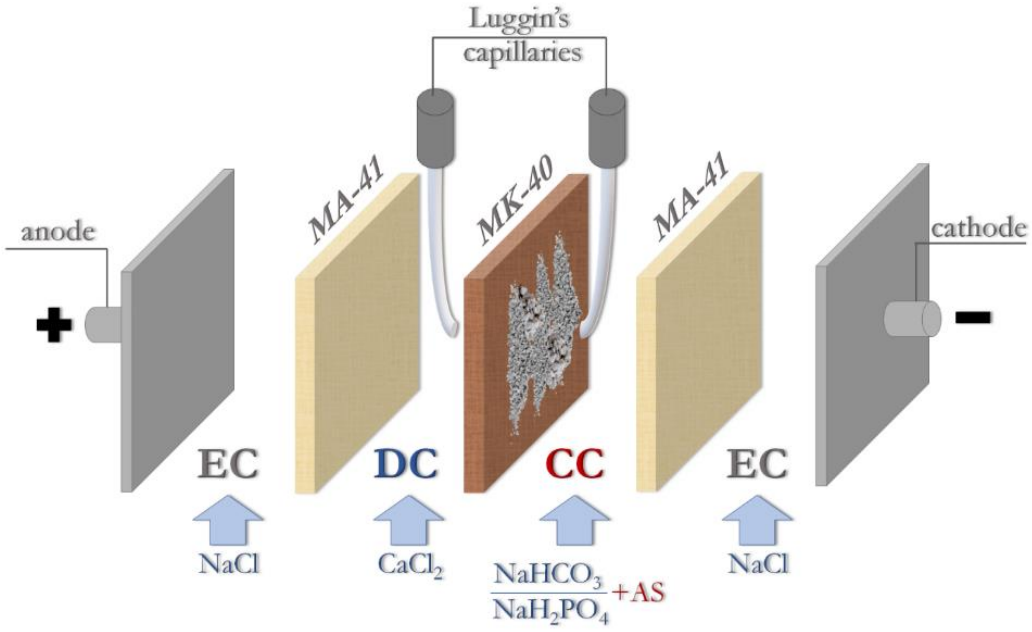

Figure 2. Principal scheme of the electrodialysis cell.

In the blank run, under the influence of an electric field, the transfer of calcium ions through the CEM leads to the formation of insoluble compound $CaCO_3$ (solubility $6.6 \cdot 10^{-4}$ g in 100 g H_2O [56]) at the membrane surface facing the CC. At the beginning of the experiment, pH of the $NaHCO_3$ solution pumped through the CC has a value of 8.43±0.05, which corresponds to *ca*. 99% HCO_3^- ions content and about 1% of CO_3^{2-} species among all forms of carbonates. Thus, with the gradual entry of Ca^{2+} ions into the CC, at some point, the product of the concentrations of Ca^{2+} and CO_3^{2-} ions exceeds the solubility product and precipitation occurs:

$$HCO_3^- + Ca^{2+} + OH^- \rightleftarrows \left[CaCO_3\right]^0 + H_2O \rightleftarrows CaCO_3^{solid} \quad (1)$$

where $[CaCO_3]^0$ corresponds to the complex of calcium with carbonate ion dissolved in aqueous phase, while $CaCO_3^{solid}$ denotes the corresponding solid phase.

Chemical speciations, described in the section 2.4, exhibit deposition of calcite at pH 8.4 in 0.04 mol/dm^3 $NaHCO_3$ solution as soon as calcium concentration exceeds 0.12 mmol/dm^3. For calcium concentration of 1 mmol/dm^3, almost 90% of calcium cations and 2% of carbonate anions are present in the solid form, capable to deposit on the membrane surface (Figure 3).

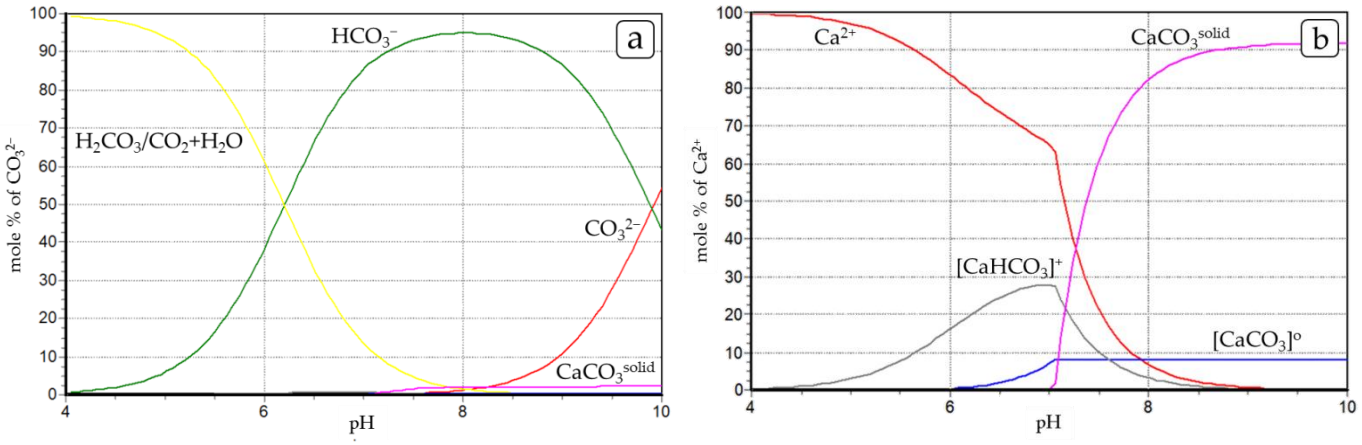

Figure 3. Mole fractions (mole %) of carbonate (a) and calcium (b) species in an aqueous solution as a function of pH at 25ºC for [CO_3^{2-}] = 0.04 mol/dm^3; [Ca^{2+}] = 1 mmol/dm^3; SPECIES software.

After the blank run, the experiments with the addition of 10^{-5} mol/dm^3 of HEDP-F, PAA-F2 or PAA-F2S to the CC have been conducted. Notably, as far as all antiscalants at pH>5 exist in aqueous phase in the anionic form, it is reasonable to add them exactly to concentration compartment. Being added to the desalination compartment, they may be removed rather fast due to transport through the AEM in an electric field. Besides, this may lead to undesirable clogging the membrane pores and deteriorating its transport properties.

In the second series, in contrast to the first series, the 0.04 mol/dm^3 NaH_2PO_4 solution (volume 4 L) is pumped through the CC. The initial pH of the NaH_2PO_4 solution is equal to 6.26±0.05. This corresponds to the mixture of $[H_2PO_4]^-$ and $[HPO_4]^{2-}$ species presence in aqueous phase. At this pH the transfer of calcium ions through the CEM leads to the formation of $CaHPO_4$ precipitate (solubility $2\cdot10^{-2}$ g in 100 g H_2O [56]). With the gradual entry of Ca^{2+} ions into the CC, at some point, the product of the concentrations of Ca^{2+} and HPO_4^{2-} ions exceeds the solubility product and precipitation occurs:

$$HPO_4^{2-} + Ca^{2+} \rightleftarrows \left[CaHPO_4\right]^0 \rightleftarrows CaHPO_4^{solid} \quad (2)$$

$$H_2PO_4^- + Ca^{2+} \rightleftarrows \left[CaHPO_4\right]^0 + H^+ \rightleftarrows CaHPO_4^{solid} \quad (3)$$

where $[CaHPO_4]^0$ corresponds to the complex of calcium with hydrophosphate ion dissolved in aqueous phase, while $CaHPO_4^{solid}$ denotes the corresponding solid phase.

The formation of another sparingly soluble phosphate $Ca_3(PO_4)_2^{solid}$ is also possible at higher pH and higher calcium concentrations even under a high excess of phosphate anions over calcium cations (Figure 4):

$$2HPO_4^{2-} + 3Ca^{2+} \rightleftarrows Ca(PO_4)_2^{solid} + 2H^+ \quad (4)$$

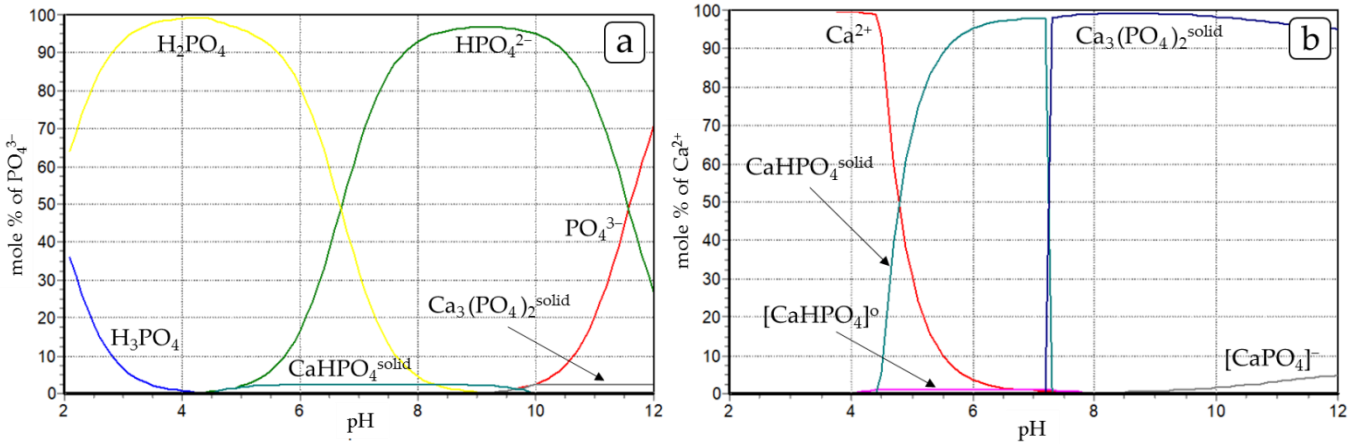

Figure 4. Mole fractions (mole %) of phosphate (a) and calcium (b) species in an aqueous solution as a function of pH at 25°C for [PO_4^{3-}] = 0.04 mol/dm^3; [Ca^{2+}] = 1 mmol/dm^3; SPECIES software.

However, the chemical speciations, described in the section 2.4, exhibit deposition of $CaHPO_4^{solid}$ (brushite) at pH<7 in 0.04 mol/dm^3 NaH_2PO_4 solution as soon as calcium concentration exceeds 0.03 mmol/dm^3. For calcium concentration of 1 mmol/dm^3, almost 95% of calcium cations (Figure 4b) and 2% of phosphate anions (Figure 4a) are present in the solid form, capable to deposit on the membrane surface. Similarly to the first series, the experiments in the absence and in the presence of ASs (10^{-5} mol/dm^3 of HEDP-F, PAA-F2 or PAA-F2S) in the CC are carried out.

During the ED experiments the pH of the solution in the CC is recorded using a pH combination electrode and pH-meter Expert 001 (Econix-Expert, Ltd., Moscow, Russia). All the experiments are conducted at 25±1°C.

2.4. Chemical speciations

Chemical equilibria modeling was performed using SPECIES software [57] and a set of stability and solubility constants, taken from the IUPAC Stability Constants Database [58]. Among these, the solubility data for calcium carbonate and calcium phosphates as well as formation constants of corresponding complexes have been selected for 20–25°C and ionic strength I = 0–0.1 mol/dm^3), Table 1. Some data represent the mean values of those, listed in [58].

Besides, an alternative interaction of calcium chelation by HEDP-F and PAA-F2 was also simulated. For this purpose the constants of hydroxyethylidene-bis(phosphonic acid), HEDP and succinic acid [58] have been used.

Table 1. Chemical equilibrium constants ($\log K$), extracted from [58] and used for chemical speciations simulation *via* software SPECIES [57] for ionic strength I = 0–0.1 mol/dm^3 and 20–25°C.

Calcium carbonate		**Calcium phosphate**	
Equilibrium	**log*K***	**Equilibrium**	**log*K***
$CO_3^{2-} + H^+ \rightleftarrows HCO_3^-$	9.90	$PO_4^{3-} + H^+ \rightleftarrows HPO_4^{2-}$	11.58
$CO_3^{2-} + 2H^+ \rightleftarrows H_2CO_3 / CO_2 + H_2O$	16.10	$PO_4^{3-} + 2H^+ \rightleftarrows H_2PO_4^-$	18.27
$CO_3^{2-} + Ca^{2+} \rightleftarrows [CaCO_3]^0$	3.4	$PO_4^{3-} + 3H^+ \rightleftarrows H_3PO_4$	20.12
$CO_3^{2-} + H^+ + Ca^{2+} \rightleftarrows [CaHCO_3]^+$	11.0	$PO_4^{3-} + Ca^{2+} \rightleftarrows CaPO_4^-$	5.2
$CO_3^{2-} + Ca^{2+} \rightleftarrows CaCO_3^{solid}$ «calcite»	–8.49	$PO_4^{3-} + Ca^{2+} + H^+ \rightleftarrows CaHPO_4$	13.22
Aragonite	–8.33	$PO_4^{3-} + Ca^{2+} + H^+ \rightleftarrows CaHPO_4^{solid}$	–18.20
vaterite	–7.99	$2PO_4^{3-} + 3Ca^{2+} \rightleftarrows Ca_3(PO_4)_2^{solid}$	–27.00
$CaCO_3^{solid}$ corresponds to calcite		$CaHPO_4^{solid}$ corresponds to brushite	

2.5. Scanning electron and fluorescence microscopy, X-ray diffraction

After the three-hour experiments on the electrodialysis processing of the solutions prone to scale deposition, the MK-40 membranes are removed from the ED cell, rinsed by deionized water and dried at ambient temperature. Then, the surfaces, facing the concentration compartment, are examined through scanning electron microscopy (SEM) and fluorescence microscopy (FM). SEM analysis is carried out using the Hitachi TM 3030 microscope (Hitachi Ltd., Tokyo, Japan) at 15 kV accelerating voltage in Charge-Up Reduction Mode and with a working distance of 4.1 mm. FM analysis is performed using the laser scanning confocal microscope LSM-710 (Carl Zeiss Microscopy, Jena, Germany), with a ×20 Plan-Apochromat objective (NA = 0.8). The fluorescence of the HEDP-F, PAA-F2, and PAA-F2S is recorded within the 470–600 nm wavelength range upon excitation by a 488 nm laser (green channel). The reflected scanning laser light is registered as an additional channel (magenta). The 3D fluorescence images are acquired with a step of 1 μm along the *Z* axis and reconstructed using ZEN software (Carl Zeiss Microscopy, Jena, Germany).

Phase composition of the deposit is characterized by powder X-ray diffraction (XRD), operating Haoyuan Instrument Co. Diffractometer (China); Cu-Kα; Ni-filter; SDD-detector Ketek. The XRD phase identification is completed using the Joint Committee on Powder Diffraction Standards (JCPDS) database, and the relative phase content is estimated with Crystallographica Search-Match software with PDF2 database.

3. Results and Discussion

3.1. Investigation of ASs effectiveness in mitigation of membrane scaling by calcium carbonate

To assess the efficacy of ASs in membrane scaling mitigation during three-hour ED experiments, a comparative analysis of MK-40 membrane chronopotentiograms (ChPs), obtained in the absence of antiscalants in the CC and in their presence, is carried out. In Figure 5, the obtained ChPs are presented in the $\Delta\varphi'$ *vs*. time (t) coordinate plane, which is a conventional form of representation, used for convenient comparison of different membrane systems. The value $\Delta\varphi'$ is defined as the difference between the measured potential drop and the ohmic potential drop that occurs in a non-polarized membrane system immediately after the current is turned on [59].

Figure 5 shows, that in the blank experiment, the PD begins to increase sharply starting from about 25 minutes. Apparently, by this time, the amount of calcium ions that have entered the CC is sufficient to exceed the solubility product of the $CaCO_3$ compound. Thus, the scale deposits are formed on the surface of the membrane due to calcium carbonate precipitation, thereby leading to the blockage of membrane pores. The formation of deposit structures on the active area of the IEM impedes the ion transport, thereby leading to an increase in resistance. Consequently, the Luggin's capillaries brought to the membrane surfaces register an increase in PD. Indeed, such an impact of scale formation on the shape of an ion-exchange membrane ChP is rather known [60–63].

A noticeable decrease in the rate of PD growth (approximately after 110 min) can be explained by the fact that by this time, probably, the entire surface of the membrane is covered with the scale layer, and further precipitate formation and deposition leads only to a gradual increase in the thickness of this layer. The latter should not lead to such a sharp increase in membrane resistance as in the case of the initial stage of membrane surface scaling, when the deposits are primarily formed on the grains of the ion-exchange resin protruding from the polyethylene surface [64] and block the ion transport pathways.

In all cases, where antiscalants are added to the CC, the growth of the PD in the ChP, associated with the scale formation on the membrane surface, begins later than in the blank experiment (Figure 5). Such effect of antiscalants has been already observed in ED systems prone to calcium sulfate scaling [51] and is anticipated, since the sub-stoichiometric antiscalants can only postpone the onset of scale formation and are not capable of entire preventing this phenomenon [65]. The exact amount of inorganic salt that exceeds thermodynamic solubility level would definitely form a solid phase.

At the same time, according to the hypothesis [46], which is mentioned in the Introduction, the prenucleation step of this solid phase formation in the bulk of the aqueous phase occurs predominantly *via* heterogeneous mechanism on nanodust particles, which act as crystallization centers. A scale inhibitor, introduced into the system, competes for these crystallization centers with calcium and carbonate ions, blocks the surface of these centers

and, consequently, obstructs dust particles for scale-forming ions sorption. A reduction in the number of nuclei leads, in turn, to the retardation of scale formation.

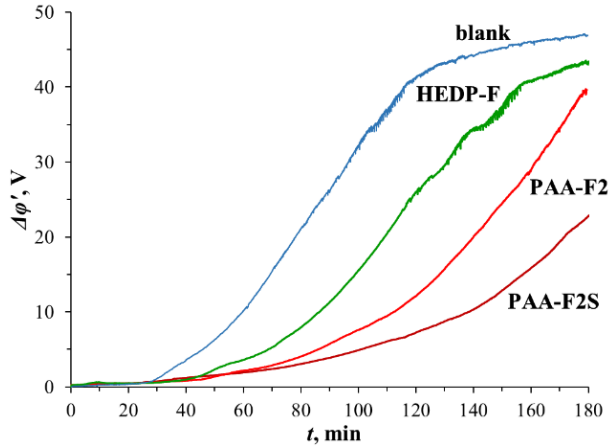

Figure 5. Chronopotentiograms of the MK-40 membrane obtained in the solutions prone to calcium carbonate scale deposition for the blank experiment and in the presence of HEDP-F, or PAA-F2, or PAA-F2S in the CC of the cell.

According to our previous studies of antiscalants activity in electrodialysis processes, the polymer AS showed a better ability to block solid nanoimpurities than the bisphosphonate AS during gypsum deposition [50, 51]. As can be seen from Figure 5, in the system under study, both polyacrylate ASs PAA-F2 and PAA-F2S also postpone the onset of active scaling process more effectively than HEDP-F. This is due to the fact that sufficiently large molecules of the studied polymer inhibitors (molecules of such polyacrylates have a length of approximately from 12 to 13 nm in a fully stretched configuration and can form rather stable aggregates with an average size of 300 nm [66]) are probably capable to block more dust particles compared to HEDP-F. The presence of sulfo groups in the structure of PAA-F2S should provide it with better dispersion in the solution, thereby increasing its effectiveness in blocking the crystallization centers. According to the results presented in Figure 5, the smallest increase in system resistance is observed in the presence of PAA-F2S, which indicates the least membrane scaling in this case. Thus, PAA-F2S has the greatest ability to mitigate calcium carbonate precipitation among all ASs studied, and the effectiveness increases in the sequence HEDP-F< PAA-F2 < PAA-F2S.

It should be noted, that the addition of inhibitors leads not only to the deferral of the moment of a sharp increase in the PD value, but also affects the slope of the ChP in the case of PAA-F2S as compared with the blank run and experiments with two other antiscalants. A decrease in the slope angle corresponds to a decrease in the rate of scale formation at the step of crystal growth. Presumably, besides the mechanism of blocking solid impurities, the reason for this may be the occurrence and contribution of other classical mechanisms of inhibition. In general, a reduction in potential drop upon addition of ASs might be provided by both: (*i*) reducing scale quantity and (*ii*) changing the morphology of scale and thus, increasing its permeability for ions.

An important factor to consider when operating an electrodialysis system at overlimiting current modes is water splitting (WS). WS arises at the interface membrane surface/depleted solution as a coupled effect of concentration polarization due to a lack of charge carriers. In the case of heterogeneous ion-exchange membranes, the major part of their surface is non-conductive (for the membranes MK-40 and MA-41, used in this study, the proportion of the conductive surface is slightly above 20% [67]), and a high value of local current density at the conductive areas of the membrane surface causes a lower electrolyte concentration there, which promotes water splitting even in underlimiting current modes [68].

In this investigation, where the ED process is carried out at currents twice above the limiting value, WS occurs intensely. In the system studied, this process contributes to a change in the pH of the solution in the considered concentration compartment. Indeed, WS at the CEM surface, facing the desalination compartment, delivers H^+ ions to the concentration compartment. The similar reaction at the AEM surface, facing the cathode compartment, provides delivery of OH^- ions. At the AEM MA-41, the WS reaction occurs more intensely than at the CEM MK-40, since the water splitting rate is governed by the catalytic participation of membrane functional groups, which accelerate protonation-deprotonation reactions of water [69, 70]. The MA-41 membrane contains a certain amount of secondary and tertiary amines, whose catalytic activity with respect to the water dissociation reaction is quite high compared to sulfo groups in the MK-40 membrane [69, 70]. Thus, the pH value in the CC should increase noticeably during the experiment. However, the alkalization of the concentrated solution during the experiments in this series turns out to be quite small (Figure 6).

This behavior of the pH in the CC during intensive WS reactions is probably explained by the buffer properties of the solution containing carbonates. Besides, the chemical equilibrium of calcium interaction with HCO_3^- anions, presented in the Equation 1, compensates partly the accumulation of OH^- ions. It is noteworthy that the addition of polyacrylate ASs has some effect on the pH value of the solution. In systems with these antiscalants, the initial pH value of the solution in the CC turns out to be lower, and during the experiment the solution pH shifts to a greater extend. The former may be explained by the fact that polyacrylate ASs contain a sufficient number of acidic groups in their structure, which can be deprotonated to release H^+ ions into the solution. The latter is probably caused by the participation of carboxyl groups, as well as of sulfo groups (in the case of PAA-F2S) of antiscalants in protonation reactions occurring locally at the CEM surface, where the local concentration of H^+ ions delivered across the membrane from its opposite side, is relatively high. In general, the measured pH value of the solution refers to the entire solution volume flowing through the CC of the cell, and this value does not reflect local pH fluctuations. Yet, these fluctuations definitely occur at the surface of the membrane under study, where scale is being formed, and might influence this process.

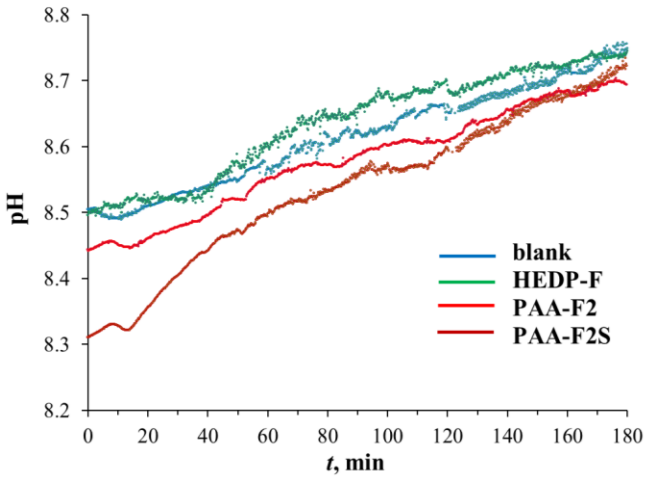

Figure 6. Time dependences of pH in the CC during ED processing of the solutions prone to calcium carbonate scale deposition for the blank experiment and in the presence of HEDP-F, or PAA-F2, or PAA-F2S in the CC of the cell.

The results of SEM and FM analysis of the surface of the membrane, facing the concentration compartment, for all experiments in the series are shown in Figure 7. The FM 3D data are presented as a superimposed image of fluorescent and reflected light, displayed in a magenta pseudo-color. The semi-quantitative results of the XRD phase composition analysis of the deposit are presented in Table 2.

Table 2. XRD calcium carbonate scale characterization results.

Experimental run	Solid phase composition
Blank	Calcite
HEDP-F	Calcite
PAA-F2	Calcite (*ca*. 58%), Vaterite (*ca*. 42%)
PAA-F2S	Calcite, nearly 100%, Vaterite (traces)

XRD of the blank experiment reveals solely calcite phase presence (large rhombohedral crystals, Figure 7a). This result is consistent with those, found earlier for calcium carbonate supersaturated solution [71–73], and with the higher thermodynamic stability of calcite relative to the other polymorphs of calcium carbonate at ambient temperature. At the same time, this phase composition is different from the calcium carbonate deposition experiment with a gradual transition from a homogeneous undersaturated solution to a supersaturated one at elevated temperature in a constant aqueous phase volume [74], where domination of aragonite over calcite phase was detected.

In the presence of HEDP-F, the deposited crystal forms of scale do not change significantly, neither in size, nor in phase composition, nor in crystal shapes relative to the blank run (Figure 7b). XRD demonstrates solely the calcite phase. The major difference

relative to the blank experiment is a distortion of significant amount of rhombohedral crystals of calcite to give the flake-like (lamellar-like) modification of calcite, indicated by blue circle at Figure 8b. Meanwhile, FM reveals a very specific and complicated location of the antiscalant on the surface of calcium carbonate (Figures 7c, 8a, b).

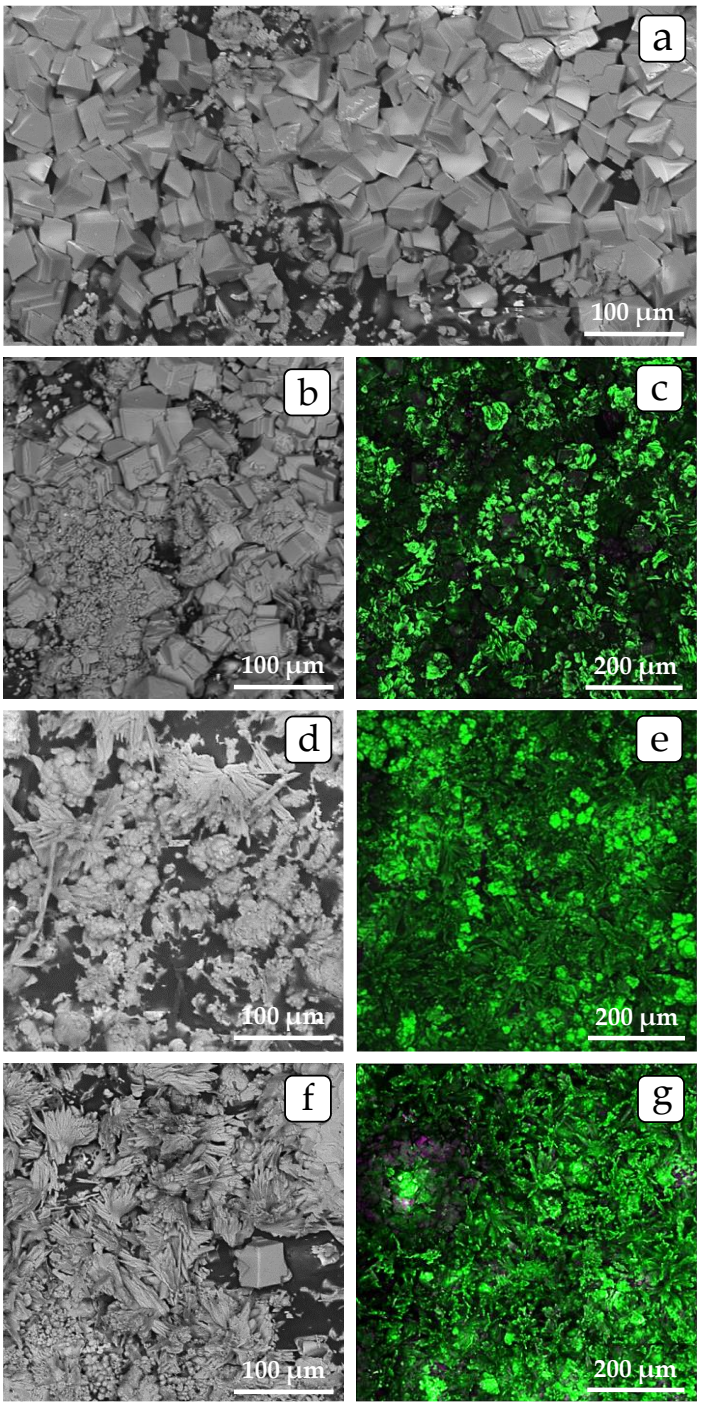

Figure 7. SEM (a, b, d, f) and FM 3D (c, e, g) images of the membrane surface facing the concentration compartment after the ED processing of the solutions prone to calcium carbonate scale deposition: blank experiment (a) and the experiments in the presence of HEDP-F (b, c), PAA-F2 (d, e), or PAA-F2S (f, g).

Figure 8 indicates that the rhombohedral calcite crystals either demonstrate no presence of HEDP-F on their surface at all (Figure 8a), or some traces of the antiscalant (Figure 8b). Notably, in most cases such traces do not concentrate on kinks, steps, or selected edges of calcite. However, the situation is quite different for the lamellar-like modification of calcite. Most of HEDP-F molecules are selectively concentrated exactly on the surface of this fraction of deposit (Figures 7c, 8a, b). Some typical flake-like calcite crystals are marked with blue circles in Figure 8b. It should be noted, that the surface of flake-like calcite crystals is covered by HEDP-F molecules rather uniformly, without special preference of kinks, steps, or selected edges for location. In addition, some HEDP-F bearing amorphous solids in the form of calcium salts CaHEDP-F might be present in the deposit [47]. These possible impurities are marked with red circle (Figure 8b).

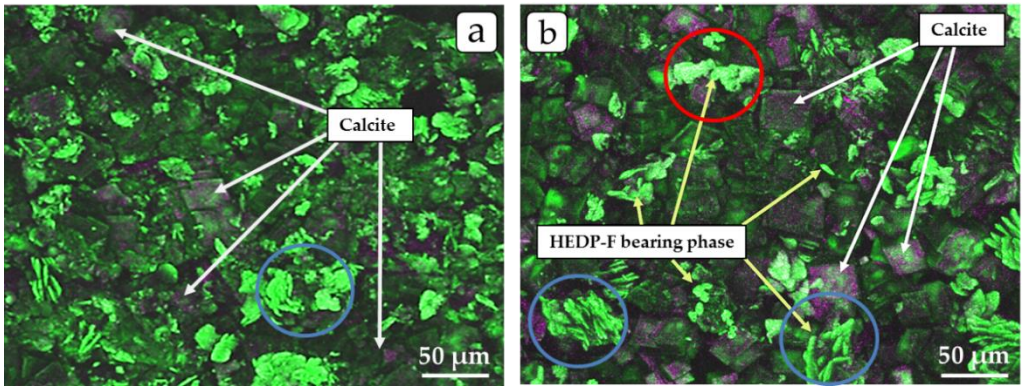

Figure 8. 3D FM images (a,b) of the $CaCO_3$ deposit on the membrane surface obtained in the presence of HEDP-F, where HEDP bearing phases denote solids other than calcite.

Thus, HEDP-F retards calcium carbonate deposition without any evident interference in the calcite rhombohedral macro-crystal growth process. Though HEDP-F is detected on the surface of flake-like crystals of calcite, such a sorption seems to have the post-crystallization character, Figure 8a, and has no relevance to the scale inhibition phenomenon. In fact, a similar behavior of HEDP-F was also registered in [74] during $CaCO_3$ deposition at elevated temperatures. At the same time, HEDP-F promotes flake-like crystals formation, and is preferably sorbed on their surface. Meanwhile, there is no clear indication that HEDP-F slows down the growth step of flake-like macro-crystals and diminishes their mean size, although it affects the nucleation step.

Unlike HEDP-F, PAA-F2 and PAA-F2S both have impact on size, phase composition and crystal shapes (Figures 7d, f; 9, 10). Indeed, the crystal habit of calcite gets changed (Figures 9, 10) and the new phase of spherical shape (vaterite) appears, Table 2. At the same time, the rhombohedral form of calcite almost escapes, while the flake-like crystals and the rod-shaped modifications of calcite are solely observed. This effect is also very common for calcium carbonate deposition in the presence of antiscalants [71–73]. Usually, this crystal habit change is broadly recognized as a major approval of scale inhibition phenomenon [35, 44, 46]. It is believed, that exactly the change in the orderly growth of a scale crystal

makes it deformed, leads to crystal structure modification and to its slower growth due to irreversible adsorption of ASs by the most active crystal growth centers (kinks, steps, or selected edges).

However, fluorescence does not prove such point of view (Figures 9, 10). One can see that fluorescent antscalants are covering the surfaces of vaterite crystals rather uniformly. No special localization of PAA-F2 and PAA-F2S molecules on kinks, steps, or selected edges of vaterite crystals is registered. Moreover, if the major contribution of scale inhibitor is really associated with the blockage of crystal growth centers, then most of antiscalant molecules, taken in substoichiometric quantities, should rather be hidden inside, but not present on the surface of already formed macro-crystals. Thus, the sorption of antiscalant on the surface of the growing vaterite crystal is likely to play the secondary role, if any, relative to the nucleation step.

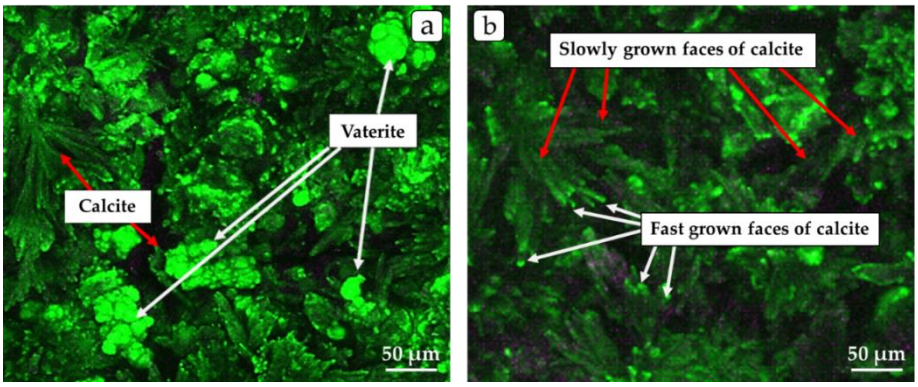

Figure 9. 3D FM images (a,b) of the $CaCO_3$ deposit on the membrane surface obtained in the presence of PAA-F2.

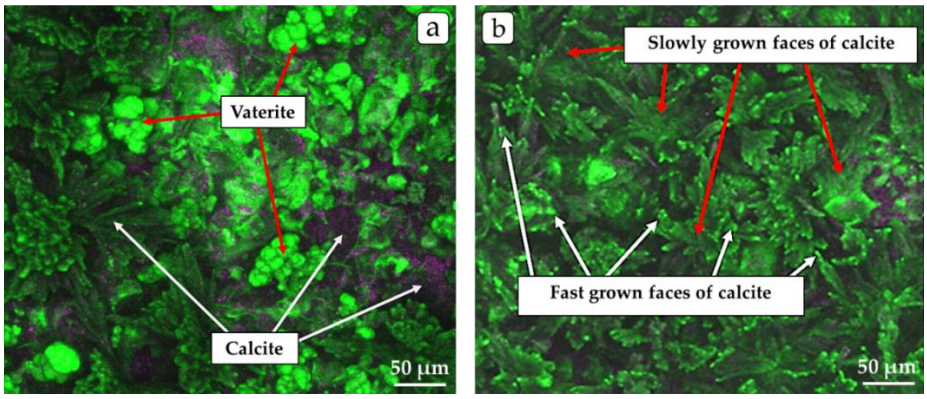

Figure 10. 3D FM images (a,b) of the $CaCO_3$ deposit on the membrane surface obtained in the presence of PAA-F2S.

At first glance, the flake-like and the rod-shaped modifications of calcite, that are deposited in the presence of PAA-F2 and PAA-F2S along with vaterite prove the hypothesis that exactly the blockage of crystal growth centers is responsible for their growth kinetics. Indeed, Figures 9 and 10 reveal a nonuniform location of antiscalant on calcite crystal

surfaces: some faces and crystal edges evidently demonstrate much higher amount of fluorescent-tagged polyacrylates than the other ones. However, the analysis of the crystal face size and the corresponding antiscalant quantity call into question the aforementioned statement. It is seen from the distribution of fluorescence on elongated rod-like crystals (Figures 9b, 10b). Evidently, the smaller section of the crystal rectangle should grow faster, then the bigger ones in order to provide elongated form. Then, it is expected that the face, that corresponds to this smaller section should be the least one covered by the antiscalant, while the other faces restraining crystal growth have to accumulate major amount of scale inhibitor. Meanwhile, the real situation is exactly the opposite one. One can see that particularly the smaller faces of calcite rods accumulate the highest amount of PAA-F2 and PAA-F2S, while the others bear much less fluorescence. Thus, it is likely, that antiscalant was sorbed post-factum, after the crystal's growth was finished. Then, the crystal face that has the highest concentration of crystal growth centers would become also the preferable place of antiscalant location after the growth process is finished.

Such a conclusion is supported by a comparison of the ChPs for the blank run and in presence of antiscalants (Figure 5). The slopes of the curves portions that may be considered corresponding to the step of macro-crystal growth ($60 < t < 110$ min for the blank run; $90 < t < 150$ min for HEDP-F, and $120 < t < 180$ min for PAA-F2) are almost the same. No significant retardation of crystal growth step by antiscalant is detected. Actually, an increase in potential drop at aforementioned periods should have a cumulative origin of both crystal nuclei growth into macrocrystals, increase of the deposit density and a corresponding decrease of the deposit layer permeability for the transport of ions. Thus, besides of crystal size, the type of crystal habit may also contribute to an increase in membrane resistance.

In this relevance, the initiation of crystal habit change by antiscalant itself might become important. Indeed, the post-factum sorption of antiscalants on crystal lattices of calcium carbonate isomorphs is capable to retard their further transformation into the thermodynamically most stable forms. For example, numerous studies have demonstrated that vaterite is formed primarily in supersaturated solutions of calcium carbonate [71]. At the same time, vaterite is the least stable phase, which is known to transfer into aragonite and then into calcite, which is the most stable. Evidently, PAA-F2 and PAA-F2S are capable to adsorb onto the surface of vaterite and slow down its further transformation into calcite in a different extent. Thus, in Figure 9 one can see quite a lot of spherical crystals of vaterite, completely covered with ASs. Meanwhile, it is not the case of HEDP-F, which fails to stabilize vaterite. Evidently, all three ASs, studied in present work, have different sorption affinity to calcite and vaterite. This phenomenon is superimposed on multistage process of deposit formation. Nevertheless, it does not seem to control the rate of solid phase formation. Indeed, the inhibition efficacy (PAA-F2S>PAA-F2>HEDP-F) does not correlate with an ability of antiscalants to stabilize vaterite (PAA-F2>PAA-F2S>HEDP-F).

3.2. Investigation of ASs effectiveness in mitigation of membrane scaling by calcium hydrogen phosphate

The results of chronopotentiometric measurements, obtained during the three-hour electrodialysis processing of solutions prone to calcium hydrogen phosphate deposition are shown in Figure 11. At the initial stage of the process (first 15–20 minutes), a sharp increase and following fairly rapid decrease in PD are observed in all experiments of this series. Such a behavior of the ChPs can be explained by the local process of formation and subsequent dissolution of scale deposits, occurring in a thin near-membrane layer of the solution at the places where the ion-exchange resin grains protrude from the membrane surface. As noted previously, a high local concentration of calcium ions in these zones can lead to very fast exceeding the solubility product and results in the formation of deposit structures on the resin grains. Moreover, due to the intense WS at the opposite side of the CEM, which ensures the flow of H^+ ions into these zones, the local pH value can be quite low. In this case, both calcium phosphate and calcium hydrogen phosphate can potentially be formed, and the precipitation of one or another compound and their ratio have a strict dependence on the pH value. Unfortunately, it is impossible to estimate the exact pH value in the near-membrane layer of the solution within the framework of our experiment. At the same time, there is no doubt that in this area the pH value will be significantly lower than in the volume of the solution in the CC (Figure 12).

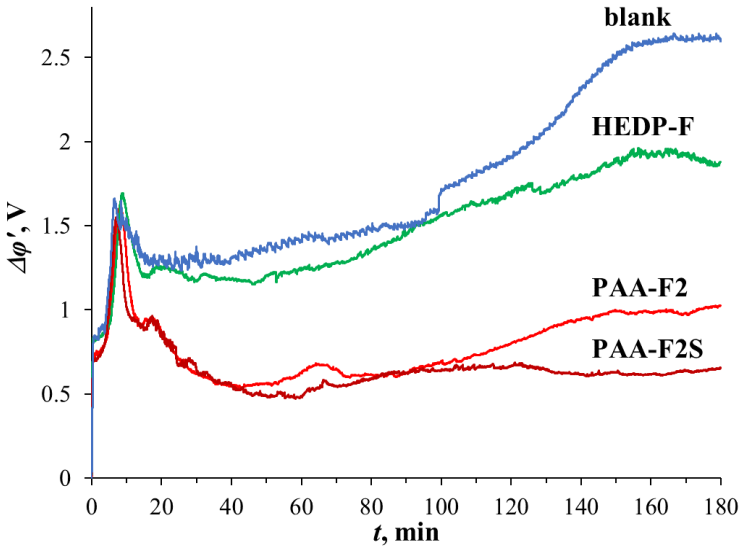

Figure 11. Chronopotentiograms of the MK-40 membrane, obtained in the solutions prone to calcium hydrogen phosphate scale deposition for the blank experiment and in the presence of HEDP-F, or PAA-F2, or PAA-F2S in the CC of the cell.

Regardless of which compound forms the deposit on the surface of the membrane, this process is reflected in the growth of the potential drop in the ChP. The subsequent decrease in PD may be caused by the dissolution of the formed deposit, which in turn is explained by

the following. Under the influence of an electric field, some phosphate ions penetrate into the CEM as co-ions and reach the CEM/depleted solution interface, where the WS reaction occurs. Phosphates have high catalytic activity in relation to the water dissociation reaction [69, 70], and even a small amount of them can be sufficient to highly intensify WS. An increase in the flux of H^+ ions arriving at the membrane surface facing the concentration compartment can lead to stronger acidification of the solution layer near the membrane surface and cause dissolution of the deposits formed on the ion-exchange resin grains. In this case, when the precipitate dissolves, calcium ions are released, which ensures the appearance of new charge carriers. In combination with the intensification of the highly mobile H^+ ions flux into the concentration compartment this may lead to the system resistance being even lower than the values preceding the moment of the scale formation onset. This reason can explain the form of the ChPs obtained in experiments with the addition of polymer antiscalants. In the case of the blank experiment and the experiment with the addition of HEDP-F, the decrease in PD associated with the dissolution of the deposit is less pronounced and is interrupted by its gradual increase. Apparently, in these systems, by this moment the active precipitation has already begun in the bulk solution itself and this process determines the shape of the ChPs. While in the case of PAA-F2 and PAA-F2S, this process is postponed due to their high ability to block solid impurities.

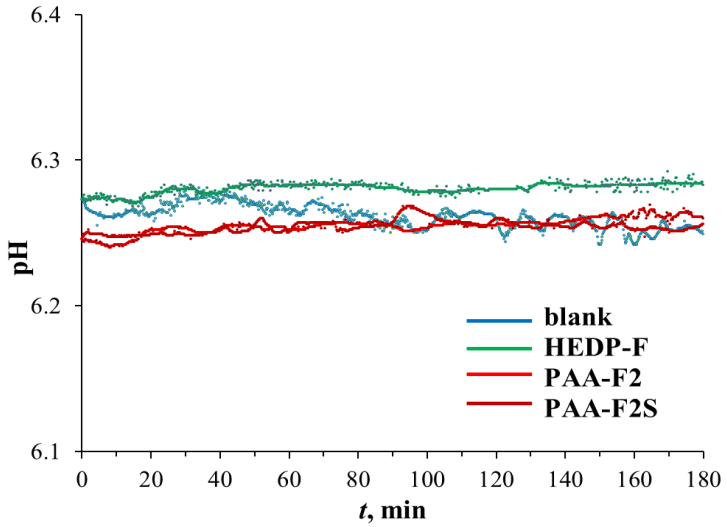

Figure 12. Time dependences of pH in the CC during ED processing of the solutions prone to calcium hydrogen phosphate scale deposition for the blank experiment and in the presence of HEDP-F, or PAA-F2, or PAA-F2S in the CC of the cell.

It should be noted that despite a sufficient amount of scale on the membrane surface at the end of the blank experiment (Figure 13a), the magnitude of potential drop does not exceed 3 V. While in the blank experiment in the first series, the formation of calcium carbonate scale results in a potential drop of almost 50 V. Probably, this contrast is due to different permeability of the deposits formed on the surface of the membranes.

Considering the kinetic dependences of pH, as in the first series, these dependences do not provide much information on ongoing processes, since the local changes in pH are leveled out due to the buffer properties of the solution containing phosphates. The initial pH value of the solutions in all experiments in this series falls within the buffer action zone (pK_2 = 7.21 [56]), as a result, no noticeable changes in the registered pH value are observed during the entire experimental run (Figure 12). Besides, the chemical equilibrium of calcium interaction with $H_2PO_4^-$ anions, presented in the equation (3), compensates partly the accumulation of OH^- ions.

In general, under the conditions of the experiments in this series, analysis of the process of scale formation and the action of ASs is a rather complex task due to the large number of factors determining the behavior of the system. However, the results, obtained in this series, correlate well with the results, obtained for the system prone to the formation of calcium carbonate precipitate: antiscalants provide reduction of membrane scaling, and their effectiveness increases in the sequence HEDP-F<<PAA-F2<PAA-F2S.

Additional information can be obtained from the results of SEM, FM (Figures 13–16) and XRD. XRD of the scale, formed on the membrane surface in the blank experiment, reveals a single crystal form in the deposit: $CaHPO_4 \cdot 2H_2O$ (brushite) deposited as large plate-like crystals. This result is quite consistent with chemical speciations diagram (Figure 4). Unlike calcium carbonate case, calcium hydrophosphate in the presence of HEDP-F, PAA-F2 and PAA-F2S also precipitates as brushite. At the same time, HEDP-F does not change the crystal habit of $CaHPO_4 \cdot 2H_2O$ (Figure 13a, b), while PAA-F2 and PAA-F2S also provide the formation of the pellet-like crystals of brushite along the plate-like ones (Figure 13d, f).

At the same time, in the presence of HEDP-F, besides of large brushite crystals, some traces of other amorphous sediment are detected. These are marked with the white arrows (Figure 14a) and are assigned to the calcium salt of HEDP-F: CaHEDP-F. Notably, the brushite crystals are covered by HEDP-F in a non-uniform manner: the flat middle part of the "plate" is free from antiscalant molecules, while the edge of the plate accumulates scale inhibitor very intensively. However, the natural fluorescence of ion-exchange resin grains, indicated by the blue arrows, Figures 14b, 15b and 16a, b is also detected.

It is worthwhile to note that PAA-F2 is observed exclusively on the surface of the plate-like crystals of $CaHPO_4 \cdot 2H_2O$, no special separate location of antiscalant being detected. PAA-F2 is distributed in a non-uniform manner both at the edges and at flat areas of "plates" (Figure 15a). At the same time, no antiscalant is observed on the surface of $CaHPO_4 \cdot 2H_2O$ pellets.

PAA-F2S demonstrates a behavior similar to PAA-F2 (Figures 13f, g, 16). PAA-F2 is also detected exclusively on the surface of plate-like crystals of $CaHPO_4 \cdot 2H_2O$, but not on the pellets.

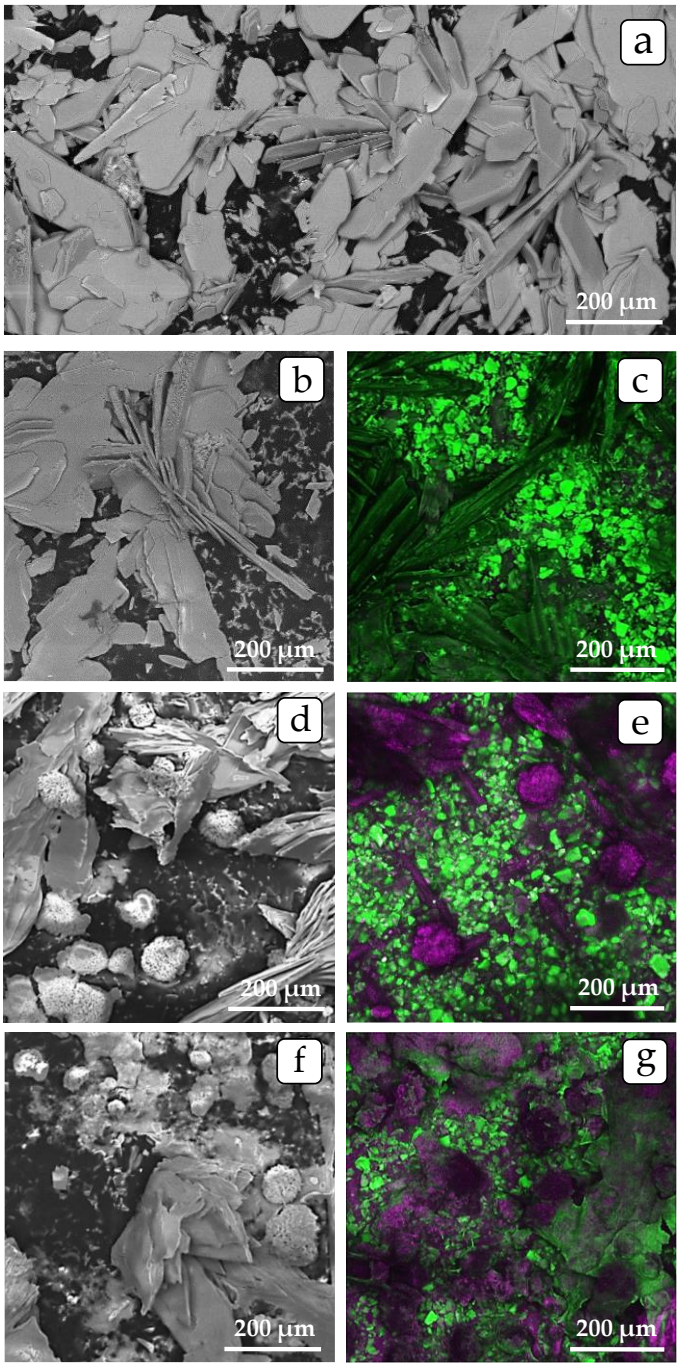

Figure 13. SEM (a, b, d, f) and FM 3D (c, e, g) images of the membrane surface facing the concentration compartment after the ED processing of the solutions prone to calcium hydrogen phosphate scale deposition: blank experiment (a) and the experiments in the presence of HEDP-F (b, c), PAA-F2 (d, e), or PAA-F2S (f, g).

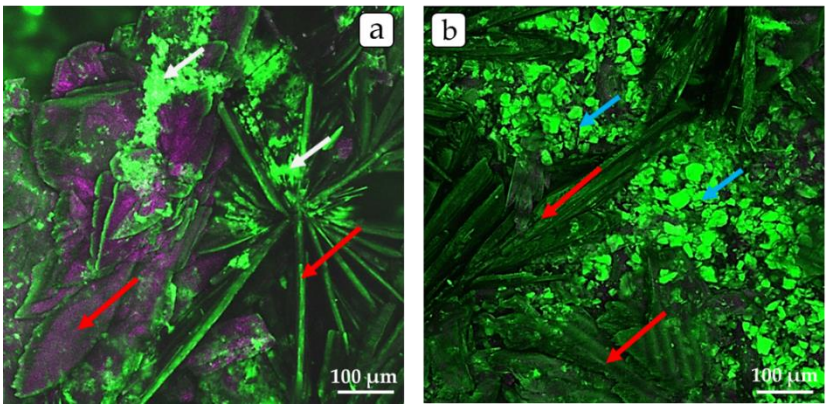

Figure 14. 3D FM images of the $CaHPO_4 \cdot 2H_2O$ crystal scrape (a) and deposit layer on the membrane surface (b) obtained in the presence of HEDP-F: the red arrows indicate the calcium phosphate crystals, the white ones – the CaHEDP-F phase, and the blue ones – the ion-exchange resin grains.

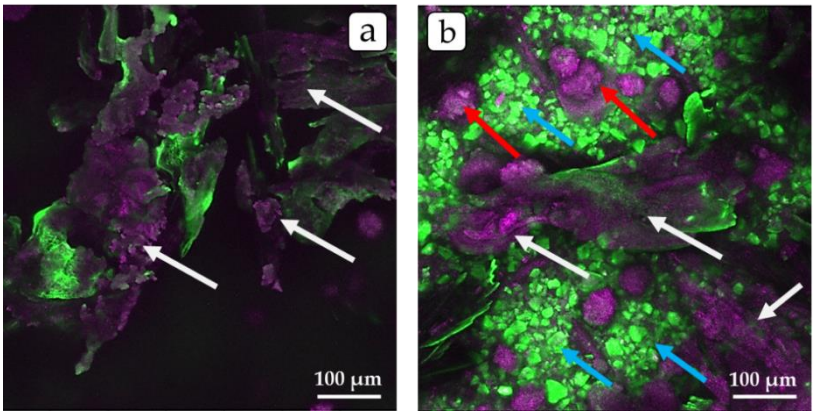

Figure 15. 3D FM images of the $CaHPO_4 \cdot 2H_2O$ deposit crystal scrape (a) and the deposit layer on the membrane surface (b) obtained in the presence of PAA-F2: the pellet-like calcium phosphate crystals, plate-like calcium phosphate crystals, and the ion-exchange resin grains are indicated by the red, white and blue arrows, respectively.

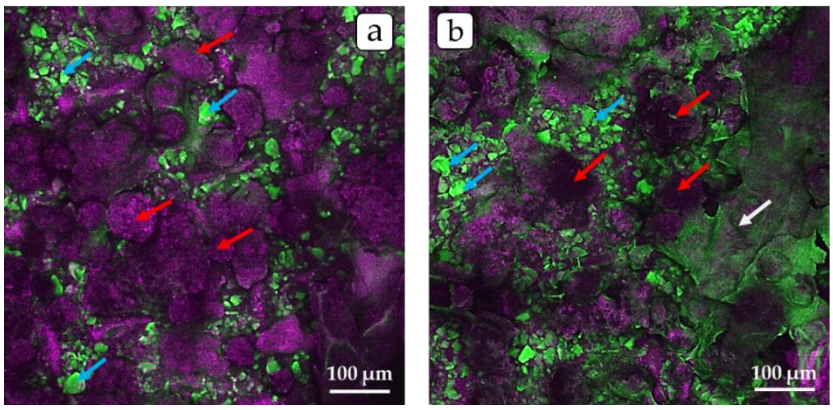

Figure 16. 3D FM images of the $CaHPO_4 \cdot 2H_2O$ deposit on the membrane surface obtained in the presence of PAA-F2S (a,b): the pellet-like calcium phosphare crystals, plate-like calcium phosphare crystals and the ion-exchange resin grains are indicated by the red, white and blue arrows, respectively.

3.3. Tentative mechanism of scale inhibition

Strictly speaking, in the present study, the term "scale inhibition" does not quite correspond to the classical concept of crystal deposition retardation. Our efforts have been focused on the practical objective to reduce the electrical resistance growth rate in the electrodialysis cell. The observed increase in potential drop is caused by membrane scaling. The extent of this increase depends both on the amount of sediment and on its permeability for the ions. Both these parameters depend on antiscalant quantity and nature, but only the former parameter corresponds to the concept "scale inhibition", while the latter one does not. Thus, one AS that provides less quantity of dense scale could be less efficient in ED than another one that allows more sediment to form, but with well permeable loose structure. Thus, the term "scale inhibition efficacy" would be used to indicate the cumulative efficiency of antiscalant in the ED process.

The results of present study indicate that, in the case of calcium carbonate, an AS mainly exhibits its inhibition activity at the step of deposit crystals nucleation. The subsequent steps of nuclei aggregation into macro-crystals, the macro-crystals growth, aggregation and deposition play the secondary role as the rate of potential drop growth in the presence of ASs is either the same (HEDP-F, PAA-F2) or slightly slower (PAA-F2S) as compared to the blank run. Thus, all the observed changes of crystal habit in the presence of ASs relative to the blank experiment have mostly concomitant character, and are not directly related to inhibition phenomenon. A similar, but less pronounced effect was detected for $CaHPO_4 \cdot 2H_2O$ deposition.

Although HEDP-F, PAA-F2 and PAA-F2S are capable to form weak soluble complexes with calcium ions, this effect is negligible. Indeed, the substoichiometric amounts of antiscalants are not capable to block a noticeable amount of calcium. Chemical speciations indicated no significant change in equilibrium diagrams in the presence of ASs. Thus, the calcium sequestration effect is not applicable in these systems.

Thus, the most realistic mechanism here is the blockage of natural solid impurities (NIs), present in any liquid [46, 47, 66, 75, 76], including the solutions circulating through the ED cell compartments. If it is assumed that exactly these impurities serve as heterogeneous crystal nucleation centers in the blank run, then the selective blockage of these impurities by ASs provides a universal explanation to all effects observed in the present study. Firstly, the HEDP-F, PAA-F2 and PAA-F2S molecules may block the surfaces of the same impurities to varying degrees. This, in turn, decreases the rates of nucleation and causes appearance of different induction times.

Secondly, the impurities are expected to be heterogeneous in nature by themselves, *e.g.* they may represent a mixture of iron hydroxo/oxides, colloidal silicon dioxide, colloidal aluminosilicates, *etc.* [75, 76]. Then, the different impurities may initiate nucleation of different calcium carbonate and calcium hydrophosphate crystallographic modifications to varying degrees. Therefore, the selective blockage of one kind of impurity by a particular

AS may lead to the selective growth of other crystallographic modifications of scale [74]. It goes without saying, that the total rate of deposit formation gets decreased.

Presumably, each kind of ASs exists in the CC both in the form of individual anions ($[H_xHEDP\text{-}F]^{(4-x)-}$, $[PAA\text{-}F2]^{x-}$, $[PAA\text{-}F2S]^{x-}$), as complexes with calcium ($[CaH_xHEDP\text{-}F]^{2-x}$, $[Ca_nPAA\text{-}F2]^{(x-2n)-}$, $[Ca_nPAA\text{-}F2S]^{(x-2n)-}$) and as sorption layers on the NIs: $[(AS)_nNI]$. The latter may be adsorbed on the surface of primarily formed crystal modification and this, in turn, slows down the further transformation of this polymorph into the more stable one. Thus, the thermodynamically unstable vaterite with the surface completely covered by either PAA-F2 or PAA-F2S forms the deposit along with more stable calcite, but it does not appear in the scale, formed in the blank run and in the presence of HEDP-F.

The selective lack of ASs on some crystal forms of scale (calcite, pellet-like crystals of $CaHPO_4 \cdot 2H_2O$) may have at least two reasons: (*i*) a low sorption affinity to the particular crystal surface, and (*ii*) the reagent is completely used up *via* sorption by the earlier formed crystal modifications.

In any case, there is no direct relationship between crystal habit modification, the real location of antiscalant on a deposit surface, and its scale inhibition efficacy. Although the present study indicated some selective location of fluorescent-tagged antiscalants on some faces and edges of both calcium carbonate and calcium phosphate crystals, these very faces appeared to provide the fastest growth, but not the other way around as the conventional inhibition theory predicts.

Possibly, the nanoimpurities nucleation/blockage concept is of broader importance and could apply to a number of other chemical reactions besides scale formation processes [77–79]. The universality of the concept should be tested, which can then lead to a novel view on both: the mechanism of crystallization and scale formation inhibition in general.

4. Conclusions

Three novel fluorescent antiscalants, PAA-F2S, PAA-F2 and HEDP-F, have been found very effective in reducing scaling on the heterogeneous cation-exchange membrane MK-40 surface in the electrodialysis treatment of the solutions prone to $CaCO_3$ and $CaHPO_4 \cdot 2H_2O$ scale formation. The following relative efficacy in $CaCO_3$ scaling retardation is registered: PAA-F2S > PAA-F2 > HEDP-F. The similar efficiency was found for $CaHPO_4 \cdot 2H_2O$ scale formation: PAA-F2S > PAA-F2 >> HEDP-F. At the same time, PAA-F2S and PAA-F2 affected the crystal habit of both $CaCO_3$ and $CaHPO_4 \cdot 2H_2O$, while HEDP-F did not. The major scaling inhibition effect was detected at the nucleation step: an increase in induction times, but no definite decrease of the crystal growth rate at the next step of deposit formation and growth was registered relative to the blank run.

Due to the unique possibility to track antiscalant location on a deposit layer *via* fluorescent marker, it is demonstrated that there is no direct relevance between scale inhibition efficacy and the ability of ASs to affect the $CaCO_3$ or $CaHPO_4 \cdot 2H_2O$ crystal growth kinetics and the crystal form of a deposit. The most contradictory effect was observed

for the elongated crystals of calcite: the face providing the fastest growth of the crystal accumulated more AS molecules, than the ones providing slower growth. Thus, no direct correlation between location of AS and crystal face growth rate is found. At the same time, in the case of vaterite, both PAA-F2 and PAA-F2S indicated a uniform coverage of the whole deposit surface without special affinity for kinks, steps, or selected edges of a crystal. In all cases, the sorption of ASs on the deposit layer likely has the post-crystallization character, and has either secondary importance or no relevance to the scale inhibition phenomenon at all. This casts doubt on a widely held theory, that exactly the change in the orderly growth of a scale crystal by ASs makes it deformed, leads to crystal structure modification and to its slower growth due to irreversible adsorption of ASs by the most active crystal growth centers (kinks, steps, or selected edges).

The observed effects are interpreted in terms of ASs interactions with natural nanoimpurities, always present in any aqueous medium and usually not taken into account by modern water treatment technologies. It appears that the major mechanism of ASs action under the conditions of an applied electric current is the same as in its absence. All the observed effects are consistently explained by molecules of antiscalant blocking impurities that act as crystallization centers, while the subsequent changes of deposit crystal modifications play the secondary role if any.

Thinking ahead, we can obtain a better understanding of crystallization pathways in general, and of their control by specialized molecules with higher affinity to nano-dust particles rather than to the chemical nature of deposit, which can possibly be adapted for the design of synthetic crystallization additives. In a parallel way, our results should attract everyone's attention to the study of the nature and properties of solid impurities, present both in natural waters and in any laboratory aqueous samples. Moreover, it appears to be possible that the presented concept of non-classical nucleation on nano-impurities is of broader significance. The principles found for crystallization pathways also apply to a variety of other chemical processes.

Acknowledgments

This research was funded by Russian Science Foundation, grant № 22-29-01035, https://rscf.ru/en/project/22-29-01035/.

The authors would like to thank the Center for collective use no. 74834 “Technological and diagnostic center for the production, research and certification of micro and nanostructures” in GPI RAS and the Center for collective use in N.S. Kurnakov Institute of General and Inorganic Chemistry of the Russian Academy of Sciences for possibility to use their equipment. A special gratitude is expressed to E.F. Popova for assistance and help with XRD analysis.

References

1. A.G. Fane, R. Wang and Y. Jia, Membrane technology: past, present and future, *Membrane and Desalination Technologies*, eds. L.K. Wang, J.P. Chen, Y.-T. Hung and N.K. Shammas, Humana Press, Totowa, NJ, USA, 2011, ch. 1, pp. 1–45. doi: 10.1007/978-1-59745-278-6_1
2. K. Elsaid, M. Kamil, E.T. Sayed, M.A. Abdelkareem, T. Wilberforce and A. Olabi, Environmental impact of desalination technologies: A review, *Sci. Total Environ*., 2020, **748**, 141528. doi: 10.1016/j.scitotenv.2020.141528
3. A. Pérez-González, A.M. Urtiaga, R. Ibáñez and I. Ortiz, State of the art and review on the treatment technologies of water reverse osmosis concentrates, *Water Res*., 2012, **46**, 267–283. doi: 10.1016/j.watres.2011.10.046
4. A.M. Lopez, M. Williams, M. Paiva, D. Demydov, T.D. Do, J.L. Fairey, Y.P.J. Lin and J.A. Hestekin, Potential of electrodialytic techniques in brackish desalination and recovery of industrial process water for reuse, *Desalination*, 2017, **409**, 108–114. doi: 10.1016/j.desal.2017.01.010
5. Y. Zhang, K. Ghyselbrecht, B. Meesschaert, L. Pinoy and B. Van der Bruggen, Electrodialysis on RO concentrate to improve water recovery in wastewater reclamation, *J. Memb. Sci*., 2011, **378**, 101–110. doi: 10.1016/j.memsci.2010.10.036
6. D. Zhao, L.Y. Lee, S.I. Ong, P. Chowdhury, K.B. Siah and H.Y. Ng, Electrodialysis reversal for industrial reverse osmosis brine treatment, *Sep. Purif. Technol*., 2019, **213**, 339–347. doi: 10.1016/j.seppur.2018.12.056
7. E. Korngold, L. Aronov and N. Daltrophe, Electrodialysis of brine solutions discharged from an RO plant, *Desalination*, 2009, **242**, 215–227. doi: 10.1016/j.desal.2008.04.008
8. G.U. Semblante, J.Z. Lee, L.Y. Lee, S.L. Ong and H.Y. Ng, Brine pre-treatment technologies for zero liquid discharge systems, *Desalination*, 2018, **441**, 96–111. doi: 10.1016/j.desal.2018.04.006
9. Y. Oren, E. Korngold, N. Daltrophe, R. Messalem, Y. Volkman, L. Aronov, M. Weismann, N. Bouriakov, P. Glueckstern and J. Gilron, Pilot studies on high recovery BWRO-EDR for near zero liquid discharge approach, *Desalination*, 2010, **261**, 321–330. doi: 10.1016/j.desal.2010.06.010
10. M.F. San Román, I. Ortiz-Gándara, E. Bringas, R. Ibañez and I. Ortiz, Membrane selective recovery of HCl, zinc and iron from simulated mining effluents, *Desalination*, 2018, **440**, 78–87. doi: 10.1016/j.desal.2018.02.005
11. Z.-Y. Guo, Z.-Y. Ji, Q.-B. Chen, J. Liu, Y.-Y. Zhao, F. Li, Z.-Y. Liu and J.-S. Yuan, Prefractionation of LiCl from concentrated seawater/salt lake brines by electrodialysis with monovalent selective ion exchange membranes, *J. Clean. Prod*., 2018, **193**, 338–350. doi: 10.1016/j.jclepro.2018.05.077
12. G. Dufton, S. Mikhaylin, S. Gaaloul and L. Bazinet, Positive impact of pulsed electric field on lactic acid removal, demineralization and membrane scaling during acid whey electrodialysis, *Int. J. Mol. Sci*., 2019, **20**, 797. doi: 10.3390/ijms20040797

13. H. Šímová, V. Kysela and A. Černín, Demineralization of natural sweet whey by electrodialysis at pilot-plant scale, *Desalin. Water Treat*., 2010, **14**, 170–173. doi: 10.5004/dwt.2010.1023
14. E. Serre, E. Rozoy, K. Pedneault, S. Lacour and L. Bazinet, Deacidification of cranberry juice by electrodialysis: Impact of membrane types and configurations on acid migration and juice physicochemical characteristics, *Sep. Purif. Technol*., 2016, **163**, 228–237. doi: 10.1016/j.seppur.2016.02.044
15. F. Gonçalves, C. Fernandes, P. Cameira dos Santos and M.N. de Pinho, Wine tartaric stabilization by electrodialysis and its assessment by the saturation temperature, *J. Food Eng*., 2003, **59**, 229–235. doi: 10.1016/S0260-8774(02)00462-4
16. M. Turek, K. Mitko, K. Piotrowski, P. Dydo, E. Laskowska and A. Jakóbik-Kolon, Prospects for high water recovery membrane desalination, *Desalination*, 2017, **401**, 180–189. doi: 10.1016/j.desal.2016.07.047
17. S. Mikhaylin and L. Bazinet, Fouling on ion-exchange membranes: Classification, characterization and strategies of prevention and control, *Adv. Colloid Interface Sci*., 2016, **229**, 34–56. doi: 10.1016/j.cis.2015.12.006
18. V.D. Grebenyuk, R.D. Chebotareva, S. Peters and V. Linkov, Surface modification of anion-exchange electrodialysis membranes to enhance anti-fouling characteristics, *Desalination*, 1998, **115**, 313–29. doi: 10.1016/S0011-9164(98)00051-4
19. S. Al-Amshawere, M.Y.M. Yunus, A.A.M. Azzodeine, D.G. Hassell, I.H. Dakhil and H.A. Hasan, Electrodialysis desalination for water and wastewater: a review, *Chem. Eng. J*., 2020, **380**, 122231. doi: 10.1016/j.cej.2019.122231
20. L. Dammak, J. Fouilloux, M. Bdiri, C. Larchet, E. Renard, L. Baklouti, V. Sarapulova, A. Kozmai and N. Pismenskaya, A review on ion-exchange membrane fouling during the electrodialysis process in the food industry, Part 1: Types, effects, characterization methods, fouling mechanisms and interactions, *Membranes*, 2021, **11**, 789. doi: 10.3390/membranes11100789
21. N. Pismenskaya, M. Bdiri, V. Sarapulova, A. Kozmai, J. Fouilloux, L. Baklouti, C. Larchet, E. Renard and L. Dammak, A review on ion-exchange membranes fouling during electrodialysis process in food industry, Part 2: Influence on transport properties and electrochemical characteristics, cleaning and its consequences, *Membranes*, 2021, **11**, 811. doi: 10.3390/membranes11110811
22. M. Bdiri, C. Larchet and L. Dammak, A review on ion-exchange membranes fouling and antifouling during electrodialysis used in food industry: Cleanings and strategies of prevention, *Chem. Afr*., 2020, **3**, 609–633. doi: 10.1007/s42250-020-00178-9
23. M. Akhter, G. Habib and S.U. Qamar, Application of electrodialysis in waste water treatment and impact of fouling on process performance, *J. Membr. Sci. Technol*., 2018, **8**, 1000182. doi: 10.4172/2155-9589.1000182

24. L.N. Nthunya, M.F. Bopape, O.T. Mahlangu, B.B. Mamba, B. Van der Bruggen, C.A. Quist-Jensen and H. Richards, Fouling, performance and cost analysis of membrane-based water desalination technologies: A critical review, *J. Environ. Management*, 2022, **301**, 113922. doi: 10.1016/j.jenvman.2021.113922
25. W.E. Katz, The electrodialysis reversal (EDR) process, *Desalination*, 1979, **28**, 31–40. doi: 10.1016/S0011-9164(00)88124-2
26. M.A.C.K. Hansima, M. Makehelwala, K.B.S.N. Jinadasa, Y. Wei, K.G.N. Nanayakkara, A.C. Herath and R. Weerasooriya, Fouling of ion exchange membranes used in the electrodialysis reversal advanced water treatment: A review, *Chemosphere*, 2021, **263**, 127951. doi: 10.1016/j.chemosphere.2020.127951
27. L.M. Camacho, J.A. Fox and J.O. Ajedegba, Optimization of electrodialysis metathesis (EDM) desalination using factorial design methodology, *Desalination*, 2017, **403**, 136–143. doi: 10.1016/j.desal.2016.07.028
28. Y. Zhang, S. Paepen, L. Pinoy, B. Meesschaert and B. Van der Bruggen, Selectrodialysis: fractionation of divalent ions from monovalent ions by novel electrodialysis, *Sep. Purif. Technol.*, 2012, **88**, 191–201. doi: 10.1016/j.seppur.2011.12.017
29. P.A. Sosa-Fernandez, J.W. Post, M.S. Ramdlan, F.A.M. Leermakers, H. Bruning and H.H.M. Rijnaarts, Improving the performance of polymer-flooding produced water electrodialysis through the application of pulsed electric field, *Desalination*, 2020, **484**, 114424. doi: 10.1016/j.desal.2020.114424
30. Q. Gao, Z. Li, C. Lei, R. Fu, W. Wang, Q. Li and Z. Liu, Application of pulsed electric field in antifouling treatment of sodium gluconate mother liquor by electrodialysis, *Materials*, 2020, **13**, 2501. doi: 10.3390/ma13112501
31. S. Mikhaylin, V. Nikonenko, G. Pourcelly and L. Bazinet, Intensification of demineralization process and decrease in scaling by application of pulsed electric field with short pulse/pause conditions, *J. Membr. Sci.*, 2014, **468**, 389–399. doi: 10.1016/j.memsci.2014.05.045
32. V.S. Nichka, T.R. Geoffroy, V. Nikonenko and L. Bazinet, Impacts of flow rate and pulsed electric field current mode on protein fouling formation during bipolar membrane electroacidification of skim milk, *Membranes*, 2020, **10**, 200. doi: 10.3390/membranes10090200
33. H.-J. Lee, S.-H. Moon and S.-P. Tsai, Effects of pulsed electric fields on membrane fouling in electrodialysis of NaCl solution containing humate, *Sep. Purif. Technol.*, 2002, **27**, 89–95. doi: 10.1016/S1383-5866(01)00167-8
34. Q. Liu, G.-R. Xu and R. Das, Inorganic scaling in reverse osmosis (RO) desalination: Mechanisms, monitoring, and inhibition strategies, *Desalination*, 2019, **468**, 114065. doi: 10.1016/j.desal.2019.07.005
35. A. Antony, J.H. Low, S. Gray, A.E. Childress, P. Le-Clech and G. Leslie, Scale formation and control in high pressure membrane water treatment systems: A review, *J. Membr. Sci.*, 2011, **383**, 1–16. doi: 10.1016/j.memsci.2011.08.054

36. I. Atamanenko, A. Kryvoruchko and L. Yurlova, Study of the scaling process on membranes, *Desalination*, 2004, **167**, 327–334. doi: 10.1016/j.desal.2004.06.142
37. L.A. Melnyk, Removal of Mn(II) compounds from water in electrodialysis desalination, *J. Water Chem. Technol*., 2015, **37**, 122–127. doi: 10.3103/s1063455x15030042
38. C. Hanrahan, L. Karimi, A. Ghassemi and A. Sharbat, High-recovery electrodialysis reversal for the desalination of inland brackish waters, *Desalin. Water Treat*., 2015, **57**, 11029–11039. doi: 10.1080/19443994.2015.1041162
39. X. Xu, L. Lin, G. Ma, H. Wang, W. Jiang, Q. He, N. Nirmalakhandan and P. Xu, Study of polyethyleneimine coating on membrane permselectivity and desalination performance during pilot-scale electrodialysis of reverse osmosis concentrate, *Sep. Purif. Technol*., 2018, **207**, 396–405. doi: 10.1016/j.seppur.2018.06.070
40. A. Elmidaoui, M.A. Menkouchi Sahli, M. Tahaikt, L. Chay, M. Taky, M. Elmghari and M. Hafsi, Selective nitrate removal by coupling electrodialysis and a bioreactor, *Desalination*, 2003, **153**, 389–397. doi: 10.1016/s0011-9164(02)01133-5
41. E.G. Darton, Membrane chemical research: centuries apart, *Desalination*, 2000, **132**, 121–131. doi: 10.1016/S0011-9164(00)00141-7
42. C. Li, Q. Yang, S. Lu and Y. Liu, Adsorption and mechanism study for phosphonate antiscalant HEDP removal from reverse osmosis concentrates by magnetic La/Zn/Fe_3O_4@PAC composite, *Colloids Surf., A*, 2021, **613**, 126056. doi: 10.1016/j.colsurfa.2020.126056
43. A. Yuchi, Y. Gotoh and S. Itoh, Potentiometry of effective concentration of polyacrylate as scale inhibitor, *Anal. Chim. Acta*, 2007, **594**, 199–203. doi: 10.1016/j.aca.2007.05.049
44. D. Hasson, H. Shemer and A. Sher, State of the art of friendly "green" scale control inhibitors: a review article, *Ind. Eng. Chem. Res*., 2011, **50**, 7601–7607. doi: 10.1021/ie200370v
45. T. Istirokhatun, M.N. Dewi, H.I. Ilma and H. Susanto, Separation of antiscalants from reverse osmosis concentrates using nanofiltration, *Desalination*, 2018, **429**, 105–110. doi: 10.1016/j.desal.2017.12.018
46. M.S. Oshchepkov and K.I. Popov, Mechanisms of scale inhibition derived from a fluorescent-tagged antiscalant visualization, *Water-Formed Deposits*, eds. Z. Amjad and K.D. Demadis, Elsevier, Amsterdam, The Netherlands, 2022, **35**, 765–782. doi: 10.1016/B978-0-12-822896-8.09988-X
47. M. Oshchepkov, S. Kamagurov, S. Tkachenko, A. Ryabova and K. Popov, An insight into the mechanisms of scale inhibition. A case study of a task-specific fluorescent-tagged scale inhibitor location on gypsum crystals, *ChemNanoMat*, 2019, **5**, 586–592. doi: 10.1002/cnma.201800660
48. M. Oshchepkov, V. Golovesov, A. Ryabova, A. Redchuk, S. Tkachenko, A. Pervov and K. Popov, Gypsum crystallization during reverse osmosis desalination of water with high sulfate content in presence of a novel fluorescent-tagged polyacrylate, *Crystals*, 2020, **10**, 309. doi: 10.3390/cryst10040309

49. Z. Zhang, M. Lu, J. Liu, H. Chen, Q. Chen and B. Wang, Fluorescent-tagged hyperbranched polyester for inhibition of $CaSO_4$ scale and the scale inhibition mechanism, *Mater. Today Commun*., 2020, **25**, 101359. doi: 10.1016/j.mtcomm.2020.101359
50. V. Gil, M. Oshchepkov, A. Ryabova, M. Trukhina, M. Porozhnyy, S. Tkachenko, N. Pismenskaya and K. Popov, Application and visualization of fluorescent-tagged antiscalants in electrodialysis processing of aqueous solutions prone to gypsum scale deposition, *Membranes*, 2022, **12**, 1002. doi: 10.3390/membranes12101002
51. V. Gil, M. Porozhnyy, M. Oshchepkov, O. Rybalkina, A. Ryabova, M. Trukhina, S. Tkachenko and K. Popov, Fluorescent-tagged antiscalants as a tool of homogeneous membrane scaling mitigation and inhibition mechanism investigation in electrodialysis processing of solutions prone to calcium sulfate precipitation, *Int. J. Corros. Scale Inhib*., 2023, **12**, 1668–1687. doi: 10.17675/2305-6894-2023-12-4-14
52. R Rautenbach and T. Albrecht, *Membrane Processes*, John Wiley & Sons, New York, 1989, 482 pp.
53. K. Popov, M. Oshchepkov, S. Kamagurov, S. Tkachenko, J. Dikareva and G. Rudakova, Synthesis and properties of novel fluorescent-tagged polyacrylate-based scale inhibitors, *J. Appl. Polym. Sci*., 2017, **134**, 45017. doi: 10.1002/app.45017
54. M. Oshchepkov, I. Solovieva, A. Menkov, S. Tkachenko, V. Udovenko and K. Popov, Continuous flow microfluidic implementation of a fluorescent marker into a polyacrylate moiety, *J. Flow Chem*., 2020, **10**, 545–550. doi: 10.1007/s41981-020-00093-7
55. G.Z. Nefedova, Z.G. Klimova and G.S. Sapoznikova, *Ion-Exchange Membranes, Granular Materials, and Powders: Catalogue*, NIITEKhim, Moscow, Russia, 1977, 32 p. (In Russian).
56. D.R. Lide, *Handbook of Chemistry and Physics*, CRC Press, Boca Raton, FL, USA, 2005.
57. *Species*, in "Solution Equilibria: principles and applications (for Windows 95, 98 and NT)", Academic Software and K.J. Powell, Sourby Old Farm, Timble, Otley, Yorks, UK, Release 1, 1999.
58. *Stability Constants Database and Mini-SCDatabase*, IUPAC and Academic Software, Sourby Old Farm, Timble, Otley, York's UK, Version 5.3, 2011.
59. H.-W. Rösler, F. Maletzki and E. Staude, Ion transfer across electrodialysis membranes in the overlimiting current range: chronopotentiometric studies, *J. Membr. Sci*., 1992, **72**, 171–179. doi: 10.1016/0376-7388(92)80197-R
60. M.C. Martí-Calatayud, M. García-Gabaldón and V. Pérez-Herranz, Mass transfer phenomena during electrodialysis of multivalent ions: chemical equilibria and overlimiting currents, *Appl. Sci*., 2018, **8**, 1566. doi: 10.3390/app8091566
61. M.A. Andreeva, N.V. Loza, N.D. Pis'menskaya, L. Dammak and C. Larchet, Influence of surface modification of MK-40 membrane with polyaniline on scale formation under electrodialysis, *Membranes*, 2020, **10**, 145. doi: 10.3390/membranes10070145

62. K.S. Barros, M.C. Martí-Calatayud, T. Scarazzato, A.M. Bernardes, D.C.R. Espinosa and V. Pérez-Herranz, Investigation of ion-exchange membranes by means of chronopotentiometry: A comprehensive review on this highly informative and multipurpose technique, *Adv. Colloid Interface Sci*., 2021, **293**, 102439. doi: 10.1016/j.cis.2021.102439
63. V.V. Gil, M.V. Porozhnyy, O.A. Rybalkina, K.G. Sabbatovskiy and V.V. Nikonenko, Modification of a heterogeneous cation-exchange membrane by Ti-Si based particles to enhance electroconvection and mitigate scaling during electrodialysis, *Electrochim. Acta*, 2021, **391**, 138913. doi: 10.1016/j.electacta.2021.138913
64. E.M. Akberova, A.M. Yatsev, E.A. Goleva and V.I. Vasil'eva, Mineral fouling on the MA-40 anion exchange membrane with the electrodialysis of strongly mineralized natural waters, *Condensed Matter and Interphases*, 2017, **19**, 451–462. doi: 10.17308/kcmf.2017.19/222
65. H. Shemer, D. Hasson and R. Semiat, Review of the state of the art of antiscalant selection, in Mineral Scales, *Biological and Industrial Systems*, ed. Z. Amjad, Taylor & Francis Group, Boca Raton, FL, USA, 2013, ch. 13, 227–256. doi: 10.1201/b15606-16
66. M. Trukhina, S. Tkachenko, A. Ryabova, M. Oshchepkov, A. Redchuk and K. Popov, Calcium sulfate crystallization in presence of fluorecent-tagged polyacrylate and some refinement of scale inhibition mechanism, *Minerals*, 2023, **13**, 559. doi: 10.3390/min13040559
67. V.I. Vasil'eva, N.A. Kranina, M.D. Malykhin, E.M. Akberova and A.V. Zhiltsova, The surface inhomogeneity of ion-exchange membranes by SEM and AFM data, *Journal of Surface Investigation. X-ray, Synchrotron and Neutron Techniques*, 2013, **7**, 144–153, doi: 10.1134/S1027451013010321
68. N.D. Pismenskaya, E.V. Pokhidnia, G. Pourcelly and V.V. Nikonenko, Can the electrochemical performance of heterogeneous ion-exchange membranes be better than that of homogeneous membranes? *J. Membr. Sci*., 2018, **566**, 54–68. doi: 10.1016/j.memsci.2018.08.055
69. R. Simons, Strong electric field effects on proton transfer between membrane-bound amines and water, *Nature*, 1979, **280**, 824–826. doi: 10.1038/280824a0
70. V.I. Zabolotskii, N.V. Shel'deshov and N.P. Gnusin, Dissociation of water molecules in systems with ion-exchange membranes, *Russ. Chem. Rev*., 1988, **57**, 801–808. doi: 10.1070/RC1988v057n08ABEH003389
71. K. Popov, G. Rudakova, V. Larchenko, M. Tusheva, E. Afanas'eva, S. Kombarova, S. Kamagurov and N. Kovaleva, A comparative performance ranking of some phosphonates and environmentally friendly polymers on $CaCO_3$ scaling inhibition by NACE protocol, *Desalination Water Treat*., 2017, **69**, 163–172.
72. P. Kjellin, X-ray diffraction and scanning electron microscopy studies of calcium carbonate deposited on a steel surface, *Colloids Surf. A*, 2003, **212**, 19–26. doi: 10.1016/S0927-7757(02)00296-0

73. G. Wolf, E. Königsberger, H.G. Schmidt, I.-C. Königsberger and H. Gamsjäger, Thermodynamic aspects of the vaterite-calcite phase transition, *J. Therm. Anal. Calorim.*, 2000, **60**, 463–472. doi: 10.1023/A:1010114131577
74. S. Tkachenko, M. Trukhina, A. Ryabova, M. Oshchepkov, S. Kamagurov and K. Popov, Fluorescent-tagged antiscalants – the new materials for scale inhibition mechanism studies, antiscalant traceability and antiscaling efficacy optimization during $CaCO_3$ and $CaSO_4 \cdot 2H_2O$ scale formation, *Int. J. Mol. Sci.*, 2023, **24**, 3087. doi: 10.3390/ijms24043087
75. M. Trukhina, K. Popov, M. Oshchepkov, S. Tkachenko, A. Vorob'eva and G. Rudakova, Impact of colloidal iron hydroxide and colloidal silicon dioxide on calcium sulfate crystallization in the presence of antiscalants, *Int. J. Corros. Scale Inhib.*, 2022, **11**, 1147–1171. doi: 10.17675/2305-6894-2022-11-3-15
76. M. Trukhina, K. Popov, M. Oshchepkov, S. Tkachenko, A. Vorob'eva and O. Guseva, Enhancement of Polyacrylate Antiscalant Activity during Gypsum Deposit Formation with the Pretreatment of Aqueous Solutions with Spruce Wood Shavings, *Materials*, 2023, **16**, 6516. doi: 10.3390/ma16196516
77. L.O. Kononov, Chemical reactivity and solution structure: on the way to a paradigm shift? *RSC Adv.*, 2015, **5**, 46718–46734. doi: 10.1039/c4ra17257d
78. D. Rak, M. Ovadova and M. Sedlaḱ, (Non)existence of bulk nanobubbles: the role of ultrasonic cavitation and organic solutes in water, *J. Phys. Chem. Lett.*, 2019, **10**, 4215−4221. doi: 10.1021/acs.jpclett.9b01402
79. L.O. Kononov, K.G. Fedina, A.V. Orlova, N.N. Kondakov, P.I. Abronina, N.M. Podvalnyy and A.O. Chizhov, Bimodal concentration-dependent reactivity pattern of a glycosyl donor: Is the solution structure involved? *Carbohydrate Res.*, 2017, **437**, 28−35. doi: 10.1016/j.carres.2016.11.009

♦ ♦ ♦